

000 001 002 003 004 005 006 007 008 009 010 011 012 013 014 015 016 017 018 019 020 021 022 023 024 025 026 027 028 029 030 031 032 033 034 035 036 037 038 039 040 041 042 043 044 045 046 047 048 049 050 051 052 053 LEARNING RECURSIVE MULTI-SCALE REPRESENTATIONS FOR IRREGULAR MULTIVARIATE TIME SERIES FORECASTING

Anonymous authors

Paper under double-blind review

ABSTRACT

Irregular Multivariate Time Series (IMTS) are characterized by uneven intervals between consecutive timestamps, which carry sampling pattern information valuable and informative for learning temporal and variable dependencies. In addition, IMTS often exhibit diverse dependencies across multiple time scales. However, many existing multi-scale IMTS methods use resampling to obtain the coarse series, which can alter the original timestamps and disrupt the sampling pattern information. To address the challenge, we propose ReIMTS, a **R**ecursive multi-scale modeling approach for **I**rrregular **M**ultivariate **T**ime **S**eries forecasting. Instead of resampling, ReIMTS keeps timestamps unchanged and recursively splits each sample into subsamples with progressively shorter time periods. Based on the original sampling timestamps in these long-to-short subsamples, an irregularity-aware representation fusion mechanism is proposed to capture global-to-local dependencies for accurate forecasting. Extensive experiments demonstrate an average performance improvement of 29.1% in the forecasting task across different models and real-world datasets. Our code is available at <https://anonymous.4open.science/r/ReIMTS-CA7B/>.

1 INTRODUCTION

Multivariate Time Series (MTS) are commonly seen in real-world applications such as healthcare, weather, and biomechanics (Zhang et al., 2023b; Shukla & Marlin, 2021). While extensive research efforts have been devoted to MTS forecasting task (Nie et al., 2022; Zhang & Yan, 2022; Yu et al., 2024), these methods often assume the input to be regularly sampled and fully observed. In reality, varying sampling rates or schedules can be applied to different series, giving rise to Irregular Multivariate Time Series (IMTS). IMTS forecasting for informed decision-making is challenging due to irregular time intervals within each variable and unaligned observations across variables, where an increasing number of studies have paid attention to (Yalavarthi et al., 2024; Zhang et al., 2024; Mercatali et al., 2024).

Under different temporal resolutions, IMTS can exhibit different patterns reflected in temporal and variable dependencies, similar to hourly, monthly, and yearly patterns in regularly sampled time series. For example, in the healthcare dataset PhysioNet'12 (Silva et al., 2012), IMTS samples contain biomarker (variable) readings for ICU patients during their first 48 hours after admission. In these samples, a 6-hour window corresponds to the common clinical monitoring period (Seymour Christopher W. et al., 2017), while a 24-hour window reflects daily cycles of patients, both of which are useful for assessing disease fluctuations (Klerman et al., 2022; Luo et al., 2025).

Although IMTS can have varying dependencies at different scales under scenarios like healthcare and weather (Menne et al., 2016), capturing them into multi-scale representations while maintaining the original sampling patterns remains challenging. On the one hand, multi-scale methods for MTS typically assume inputs to be regularly sampled and fully observed (Shabani et al., 2022; Wang et al., 2023; Chen et al., 2023), which are not well-suited for IMTS. On the other hand, multi-scale methods for IMTS are still underexplored (Zhang et al., 2023a; Luo et al., 2025; Marisca et al., 2024). These multi-scale IMTS methods often involve resampling to obtain a coarse-grain series, which balances the number of observations across different variables but may disrupt the original sampling pattern.

054 As depicted in Figure 1, the upper sample is from the healthcare dataset PhysioNet’12, while the
 055 lower one is downsampled using the same way as (Zhang et al., 2023a). Variable Bilirubin in the
 056 original sample shows relatively dense observations in the first 12 hours and sparse observations in
 057 the subsequent 36 hours, indicating careful monitoring of disease progression at the beginning of
 058 ICU admission (Lakshman et al., 2025; Holford, 2019; Morrill et al., 2020). After downsampling to
 059 the coarse series, the dense-to-sparse sampling pattern of variable Bilirubin is disrupted, affecting
 060 subsequent dependency learning. Additionally, the disruption of urgent to mild clinical monitoring
 061 information is disrupted, where information obtained through more frequent monitoring could be
 062 beneficial for early clinical decision-making (Miller et al., 2007).

063 To preserve essential sampling pattern information
 064 during multi-scale dependency learning in
 065 the above scenarios, we propose ReIMTS, a
 066 recursive multi-scale approach for IMTS fore-
 067 casting. At each scale level, ReIMTS splits
 068 an IMTS sample into smaller subsamples with
 069 shorter time periods, while maintaining the
 070 original sampling timestamps for all observa-
 071 tions and thus preserving the original sampling
 072 pattern. By recursively splitting the sample in
 073 a top-down manner, input IMTS are viewed
 074 from a global to local perspective. Each back-
 075 bone captures dependencies within a specific
 076 scale level, and learned latent representations
 077 are transferred from higher scale levels to lower
 078 ones. Leveraging global-to-local multi-scale rep-
 079 resentations learned from preserved sampling
 080 patterns, ReIMTS employs an irregularity-aware
 081 fusion mechanism to capture semantics across
 082 different scales, thereby providing accurate fore-
 083 casting results. Moreover, ReIMTS is compati-
 084 ble with most existing IMTS models due to
 085 its flexible architectural design, boosting their
 086 forecasting performance in a plug-and-play way.

086 Our main contributions are as follows:

- 087 • We introduce recursive splitting based on time periods for IMTS samples to preserve the
 088 original sampling patterns across all scale levels, and leverage IMTS backbones to capture
 089 dependencies in different time periods as multi-scale representations.
- 090 • We propose ReIMTS, a recursive multi-scale method for IMTS forecasting. Using
 091 irregularity-aware representation fusion, it recursively captures global-to-local dependencies
 092 and provides accurate predictions.
- 093 • Extensive experiments including twenty-six baseline methods and five IMTS datasets on
 094 IMTS forecasting are conducted. Tested on six IMTS backbones, ReIMTS consistently
 095 boosts their forecasting performance in all settings while maintaining good efficiency.

097 2 RELATED WORK

100 2.1 IRREGULAR MULTIVARIATE TIME SERIES FORECASTING

101 In recent years, an increasing number of studies have paid attention to IMTS forecasting (Yalavarthi
 102 et al., 2024; Zhang et al., 2024; Mercatali et al., 2024). From a model architecture perspective,
 103 methods for IMTS modeling can be broadly categorized into RNN-based (Che et al., 2018; Shukla &
 104 Marlin, 2018), ODE-based (Rubanova et al., 2019; Biloš et al., 2021; Mercatali et al., 2024), GNN-
 105 based (Yalavarthi et al., 2024; Zhang et al., 2021; Luo et al., 2025), Set-based (Horn et al., 2020),
 106 Diffusion-based (Tashiro et al., 2021), and Transformer-based (Zhang et al., 2023a). While a variety
 107 of model architectures have been employed in IMTS modeling, most of them follow the encoder-
 decoder structure. Therefore, inputs for their decoders can include temporal representations (Che

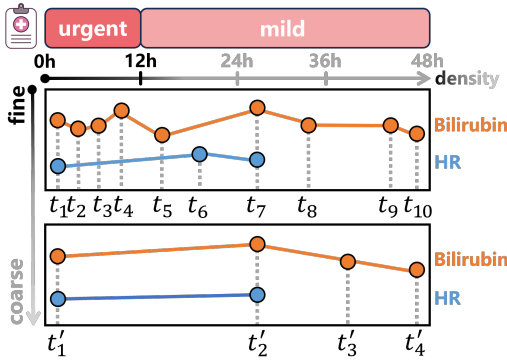


Figure 1: Existing multi-scale methods for IMTS resample the coarse series to balance differences in sampling densities across different variables. In the original sample from the healthcare dataset PhysioNet’12, liver function marker Bilirubin and heart rate (HR) exhibit a dense-to-sparse sampling pattern reflecting urgent to mild clinical monitoring, which is disrupted in the coarse series.

108 et al., 2018; Shukla & Marlin, 2018; Rubanova et al., 2019; Biloš et al., 2021; Mercatali et al.,
 109 2024), variable representations (Luo et al., 2024; Zhang et al., 2024; Luo et al., 2025; Marisca et al.,
 110 2024), observation representations (Yalavarthi et al., 2024; Zhang et al., 2021; Horn et al., 2020), or
 111 combinations thereof.
 112

113 2.2 MULTI-SCALE MODELING FOR TIME SERIES 114

115 Existing methods for regularly sampled time series have widely adopted multi-scale information
 116 during modeling for accurate predictions. From a sampling pattern perspective, Pyraformer (Liu et al.,
 117 2021), NHITS (Challu et al., 2023), Scaleformer (Shabani et al., 2022), and TimeMixer (Wang et al.,
 118 2023) use embedding merging or resampling that disrupts original observed timestamps to obtain
 119 different scales, potentially missing out on sampling pattern information. Pathformer (Chen et al.,
 120 2023) and MOIRAI (Woo et al., 2024) segment time series based on the number of observations
 121 rather than time periods, which cannot preserve the sampling rate information. TAMS-RNNs (Chen
 122 et al., 2021) was designed based on RNNs for regularly sampled time series, thus not well adapted
 123 for IMTS. Multi-scale modeling in IMTS methods is relatively underexplored. Warpformer (Zhang
 124 et al., 2023a), Hi-Patch (Luo et al., 2025), and HD-TTS (Marisca et al., 2024) address irregularities
 125 within IMTS, but they also employ resampling to get different scales and still cannot preserve the
 126 original sampling patterns.
 127

128 3 PROBLEM DEFINITION

129 With a total of T timestamps and V variables, an IMTS sample can be denoted as a set containing
 130 Y observation tuples $\mathbf{S} := \{(t_i, z_i, v_i) | i = 1, \dots, Y\}$, where $t_i \in \{0, \dots, T\}$, $z_i \in \mathbb{R}$, and $v_i \in$
 131 $\{1, \dots, V\}$ represents the timestamp, observed value, and variable indicator respectively. For the IMTS
 132 forecasting task, the set of forecast queries $\mathbf{Q} := \{q_j | j = 1, \dots, Y_Q\}$ containing Y_Q observations is
 133 derived by combining (t_j, v_j) of the j -th observation tuple within the forecast window. We aim to
 134 learn a forecasting model $\mathcal{F}(\cdot)$, such that given an input IMTS sample \mathbf{S} and a forecast query \mathbf{Q} as
 135 input, it accurately predicts the corresponding observed values \mathbf{Z} :
 136

$$\mathcal{F}(\mathbf{S}, \mathbf{Q}) \rightarrow \mathbf{Z}. \quad (1)$$

140 4 METHODOLOGY

141 The overview of our proposed method, ReIMTS, is illustrated in Figure 2. We first explain how
 142 to learn representations recursively at different scale levels in Section 4.1. Subsequently, we detail
 143 the irregularity-aware representation fusion in Section 4.2. Training loss design is described in
 144 Section 4.3. Finally, we discuss the differences between our method and existing approaches in
 145 Section 4.4. Details on the operations are available at Algorithm 1. Further discussion of how
 146 backbones address irregularities and forecast-related queries can be found in the Appendix C.
 147

148 4.1 RECURSIVE LEARNING ACROSS SCALES IN IMTS

149 In this section, we explain the methods for obtaining representations at each scale level, and how
 150 we ensure that the shape of global representations at the current scale matches the shape of local
 151 representations in the subsequent scale. It should be noted that in the following discussion, ‘global’
 152 and ‘local’ are used to describe relative scales between upper and lower levels, rather than considering
 153 all N levels. During data preprocessing, we align the raw multivariate time series within each sample
 154 \mathbf{S} based on timestamps to obtain the zero-padded sample $\mathbf{S}^1 \in \mathbb{R}^{L^1 \times V}$ at scale level 1, where L^1
 155 is the maximum number of observations in a univariate time series. Also, a corresponding mask
 156 $\mathbf{M}^1 \in \{0, 1\}^{L^1 \times V}$ is created, indicating actual observations with 1s and zero-padded values with 0s.
 157 As shown in the left panel of Figure 2, for each scale level $n \in \{1, \dots, N\}$ among the total N levels,
 158 an IMTS sample \mathbf{S}^1 is recursively partitioned by time periods to generate a series of subsamples. At
 159 scale level n , we denote the length of time period as T^n , the number of subsamples as $P^n = \frac{T^1}{T^n}$,
 160 and the maximum number of observations in a univariate time series after splitting and zero padding
 161

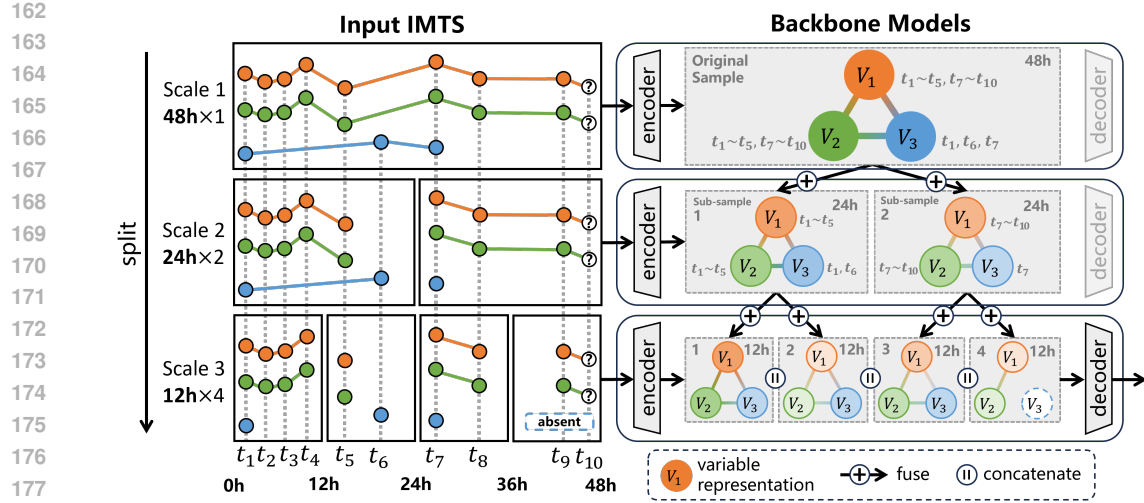


Figure 2: The architecture of ReIMTS with three scale levels. For the original IMTS sample on the top left, ReIMTS recursively splits it into subsamples with shorter time periods at each scale level. ReIMTS is compatible with most IMTS models, and we use graph neural networks as backbones here to illustrate multi-scale variable representation learning. Local representations from lower scale levels are fused with global ones from upper scale levels. The decoder in the lowest scale concatenates representations and decodes them into forecast predictions.

as L^n . For the k -th subsample $s(t_k^n)$ with $k \in \{1, \dots, P^n\}$, its time period consists of the timestamps $t_k^n = \{t | T^n(k-1) < t \leq T^n k\}$. Therefore, the set of all subsamples at scale level n can be written as:

$$\mathbf{S}^n := \{s(t_k^n)\}_{k=1}^{P^n}, \quad (2)$$

where $\mathbf{S}^n \in \mathbb{R}^{P^n \times L^n \times V}$. The mask is splitted in the same way to obtain \mathbf{M}^n . It should be noted that L^n and T^n are distinct: whereas T^n incorporates real-world time units such as minutes, hours, or years, L^n merely denotes the number of observations without any time units. It should also be noted that the split position is based on time periods rather than an equal number of observations, where the term ‘observation’ includes both actual observed values and zero-padded values used for alignment. As noted in previous studies (Chowdhury et al., 2023; Zhang et al., 2024), splitting IMTS samples based on the number of observations can result in subsamples that correspond to different time lengths in reality. This can affect the learning of varying sampling density information in the original data. Therefore, we use a time period splitting approach to preserve the sampling information across all scale levels. The specific time periods chosen for each dataset are described in Appendix B.2.

At scale level n , the IMTS backbone $\mathcal{F}^n(\cdot)$ uses its encoder $\mathcal{F}_{\text{enc}}^n(\cdot)$ to obtain latent representations \mathbf{E}^n of input subsamples \mathbf{S}^n :

$$\mathbf{E}^n = \mathcal{F}_{\text{enc}}^n(\mathbf{S}^n). \quad (3)$$

The definition of the encoder can vary across different IMTS backbones, with our implementation details provided in Appendix C. For most existing IMTS models, latent representations fall into three categories $\mathbf{E}^n \in \{\mathbf{E}_{\text{time}}^n, \mathbf{E}_{\text{var}}^n, \mathbf{E}_{\text{obs}}^n\}$: temporal representations $\mathbf{E}_{\text{time}}^n \in \mathbb{R}^{P^n \times L^n \times D}$, variable representations $\mathbf{E}_{\text{var}}^n \in \mathbb{R}^{P^n \times V \times D}$, and observation representations $\mathbf{E}_{\text{obs}}^n \in \mathbb{R}^{P^n \times L^n \times V \times D}$. Here, D denotes the hidden dimension.

During subsequent processing, \mathbf{E}^n is first transformed into \mathbf{G}^n through irregularity-aware representation fusion, and then reshaped into \mathbf{H}^n to match the shape of \mathbf{E}^{n+1} at the next scale. To compute \mathbf{G}^n from \mathbf{E}^n , we incorporate global representations from the upper scale when $n > 1$, as detailed in Section 4.2. For $n = 1$, we simply set $\mathbf{G}^1 = \mathbf{E}^1$. Accordingly, \mathbf{G}^n also consists of the three types $\mathbf{G}^n \in \{\mathbf{G}_{\text{time}}^n, \mathbf{G}_{\text{var}}^n, \mathbf{G}_{\text{obs}}^n\}$, each retaining the same shape as its corresponding counterpart in \mathbf{E}^n . To further obtain \mathbf{H}^n from \mathbf{G}^n , we follow the implementation described in Appendix A. Specifically, we split along the temporal dimension for temporal or observation representations, yielding $\mathbf{H}_{\text{time}}^n$ or $\mathbf{H}_{\text{obs}}^n$, and apply duplication for variable representations to obtain $\mathbf{H}_{\text{var}}^n$. The resulting output

216 $\mathbf{H}^n \in \{\mathbf{H}_{\text{time}}^n, \mathbf{H}_{\text{var}}^n, \mathbf{H}_{\text{obs}}^n\}$ at scale n is then provided to scale $n + 1$ as its global representation. In
 217 the following section, we discuss how global-to-local representations are recursively fused across
 218 scales.

219

220 4.2 IRREGULARITY-AWARE REPRESENTATION FUSION
 221

222 In this section, we introduce the irregularity-aware recursive fusion of global-to-local representations.
 223 At the lower scale level $n + 1$, we want to evaluate the importance of the global representation
 224 \mathbf{H}^n from upper scale level n , while accounting for the inherent irregularity in the original IMTS.
 225 Therefore, a lightweight scoring layer is utilized to assign weights α to the global representation \mathbf{H}^n .
 226 Moreover, the binary mask \mathbf{M}^{n+1} is also used to indicate irregularity.

227
$$\mathbf{H}_{\text{IMTS}}^n = \begin{cases} \mathbf{H}^n \cdot \mathbf{M}^{n+1}, & \text{when } \mathbf{H}^n = \mathbf{H}_{\text{time}}^n \text{ or } \mathbf{H}_{\text{obs}}^n \\ \mathbf{H}^n, & \text{when } \mathbf{H}^n = \mathbf{H}_{\text{var}}^n \end{cases}, \quad (4)$$

228
$$\alpha = \text{ReLU}(\text{FF}(\mathbf{H}_{\text{IMTS}}^n)), \quad (5)$$

229 where ReLU is the non-linear activation function and FF is a feed-forward layer. It should be noted
 230 that the irregularity information for variable representations $\mathbf{H}_{\text{var}}^n$ has been encoded by the encoders
 231 of IMTS backbones, while padding values are still present in observation representations $\mathbf{H}_{\text{time}}^n$ and
 232 $\mathbf{H}_{\text{obs}}^n$. Therefore, we use the mask \mathbf{M}^{n+1} to distinguish between observations and padding values
 233 specifically in temporal and observation representations. The score α is then used to fuse the local
 234 representation \mathbf{E}^{n+1} and global one:

235
$$\mathbf{G}^{n+1} = \mathbf{E}^{n+1} + \alpha \mathbf{H}_{\text{IMTS}}^n. \quad (6)$$

236

237 4.3 TRAINING OF REIMTS
 238

239 In this section, we introduce the process for obtaining forecast values and training ReIMTS. At the
 240 lowest scale level N , the decoder of IMTS backbone \mathcal{F}_{dec} takes the concatenated representation as
 241 input and predicts the forecast values $\hat{\mathbf{Z}}$:

242
$$\hat{\mathbf{Z}} = \mathcal{F}_{\text{dec}}(\text{Concat}(\{\mathbf{G}^n\}_{n=1}^N)), \quad (7)$$

243 where the definition of decoder is the subsequent network modules after the encoder of IMTS
 244 backbone, and Concat denotes the concatenation of representations from the same sample. For a
 245 detailed explanation of the backbone decoder’s structure, please refer to Appendix C. The model
 246 is trained by minimizing the Mean Squared Error (MSE) loss between the predicted values $\hat{\mathbf{Z}}$ for
 247 forecast queries and their corresponding ground truth \mathbf{Z} :

248
$$\mathcal{L} = \frac{1}{Y_Q} \sum_{j=1}^{Y_Q} (\hat{z}_j - z_j)^2. \quad (8)$$

249 It should be noted that only forecast queries are used in loss calculations, which is implemented by
 250 multiplying prediction $\hat{\mathbf{Z}}$ and binary masks $\mathbf{M}_Q \in \{0, 1\}^{L_Q \times V}$ corresponding to the forecast horizon
 251 L_Q .

252

253 4.4 DELINEATING FROM EXISTING METHODS
 254

255 We discuss the differences and similarities between ReIMTS and existing approaches in this section,
 256 and depicted in Figure 3. Patch-based methods, such as tPatchGNN (Zhang et al., 2024) and
 257 PrimeNet (Chowdhury et al., 2023), can be viewed as variants of ReIMTS with only one scale level.
 258 Although they split samples based on time periods, tPatchGNN and PrimeNet are limited to a single
 259 time period length during training. In contrast, ReIMTS can choose varying lengths at different
 260 scale levels, allowing for the exploration of richer multi-scale dependencies. Moreover, ReIMTS
 261 is a plug-and-play method that seamlessly works with most encoder-decoder IMTS backbones.
 262 It should be noted that tPatchGNN and PrimeNet learn global dependencies through inter-patch
 263 learning, while ReIMTS learns from its upper scale levels. Compared to multi-scale methods for

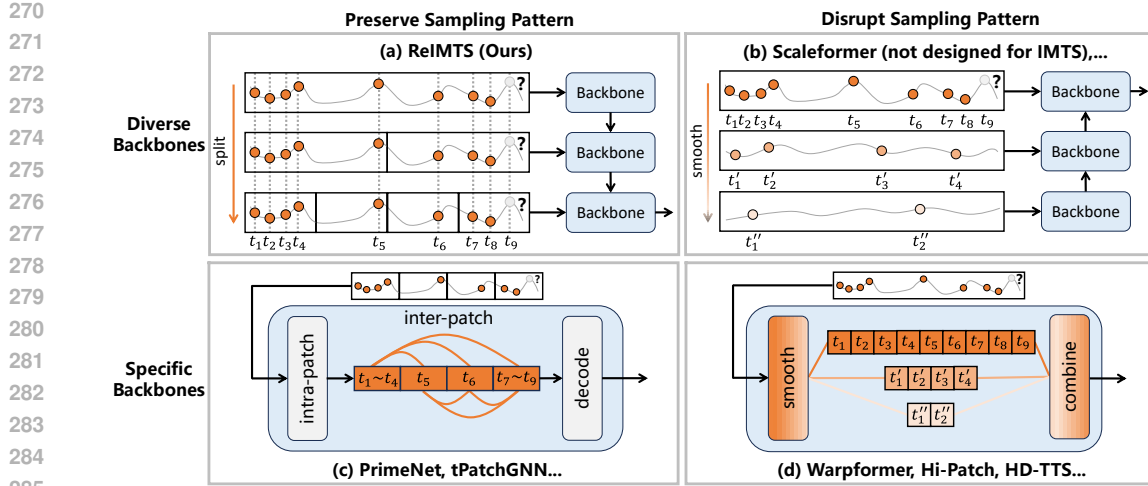


Figure 3: Comparison of our method and existing approaches. (a) ReIMTS preserves the original sampling pattern while remaining compatible with most IMTS backbones. (b) Sample-space resampling methods. (c) Patch-based methods for IMTS. (d) Representation-space resampling methods.

Table 1: Summary of five irregular time series datasets.

Description	MIMIC-III	MIMIC-IV	PhysioNet'12	Human Activity	USHCN
Max length	96	971	47	131	337
# Variable	96	100	36	12	5
# Sample	21,250	17,874	11,981	1,359	1,114
Avg # obs.	144.6	304.8	308.6	362.2	313.5
Avg # obs. (padding)	9,216.0	92,000.0	1,692.0	1,573.2	1,685.0

regularly sampled time series such as Pathformer (Chen et al., 2023), MOIRAI (Woo et al., 2024), and Scaleformer (Shabani et al., 2022), the assumption of regular sampling and division by the number of observations makes them not well-suited, as described in Section 4.1. Furthermore, Pathformer and MOIRAI require slow transformer-based layers, whereas ReIMTS can utilize lightweight IMTS backbones such as GraFITi (Yalavarthi et al., 2024) or mTAN (Shukla & Marlin, 2020). Scaleformer uses resampling to obtain multi-scale inputs, which can disrupt the sampling pattern information, as discussed in Section 1.

5 EXPERIMENTS

5.1 EXPERIMENTAL SETUP

5.1.1 DATASETS

Five widely studied irregular multivariate time series datasets, covering healthcare, biomechanics, and climate, are used in the experiments. Their statistics are summarized in Table 1. MIMIC-III (Johnson et al., 2016) is a clinical database collected from ICU patients during the initial 48 hours of admission, which is rounded for 30 minutes. MIMIC-IV (Johnson et al., 2023) is built upon MIMIC-III, which has a higher sampling frequency and data are rounded for 1 minute. PhysioNet'12 (Silva et al., 2012) is also a clinical database collected during the first 48 hours of ICU stay, rounded for 1 hour. Human Activity includes biomechanical data detailing 3D positional variables, which are rounded for 1 millisecond. USHCN (Menne et al., 2016) includes climate data spanning over 150 years, collected from meteorological stations distributed across the United States. Our analysis focuses on a subset of 4 years between 1996 and 2000. For all five datasets, we follow the preprocessing setup provided in the publicly available code pipeline PyOmniTS (Li et al., 2025), which originated from GraFITi and tPatchGNN (Yalavarthi et al., 2024; Zhang et al., 2024). It splits datasets into training, validation,

324
 325 Table 2: Experimental results for our method (**+ReIMTS**) with respective baselines, evaluated by
 326 MSE (mean \pm std) $\times 10^{-1}$ on five irregular multivariate time series datasets. The best results are
 327 indicated in **bold**. Average improvements (error reductions) are marked with \uparrow .
 328

	Algorithm	MIMIC-III	MIMIC-IV	PhysioNet'12	Human Activity	USHCN	Vs Ours
330	PrimeNet	original +ReIMTS	9.04 \pm 0.00 4.76 \pm 0.19	6.25 \pm 0.00 3.58 \pm 0.03	7.93 \pm 0.00 3.01 \pm 0.03	26.84 \pm 0.02 0.82 \pm 0.02	3.66 \pm 0.01 1.37 \pm 0.09 \uparrow 62.3%
331	mTAN	original +ReIMTS	8.51 \pm 0.14 6.37 \pm 0.05	5.09 \pm 0.12 4.04 \pm 0.10	3.75 \pm 0.02 3.51 \pm 0.02	0.89 \pm 0.03 0.89 \pm 0.01	1.93 \pm 0.02 1.23 \pm 0.03 \uparrow 17.7%
332	TimeCHEAT	original +ReIMTS	4.41 \pm 0.05 4.40 \pm 0.03	2.50 \pm 0.01 2.02 \pm 0.03	3.27 \pm 0.11 2.90 \pm 0.01	0.68 \pm 0.04 0.52 \pm 0.01	2.97 \pm 0.29 1.24 \pm 0.06 \uparrow 22.5%
333	GRU-D	original +ReIMTS	4.75 \pm 0.04 4.67 \pm 0.05	5.97 \pm 0.22 3.91 \pm 0.10	3.25 \pm 0.00 3.25 \pm 0.00	1.76 \pm 0.23 0.51 \pm 0.01	1.58 \pm 0.04 1.49 \pm 0.02 \uparrow 22.6%
334	Raindrop	original +ReIMTS	5.13 \pm 0.02 5.05 \pm 0.06	3.41 \pm 0.05 2.95 \pm 0.06	3.27 \pm 0.01 3.14 \pm 0.01	0.89 \pm 0.02 0.87 \pm 0.00	2.13 \pm 0.07 1.53 \pm 0.06 \uparrow 9.9%
335	GraFITi	original +ReIMTS	3.70 \pm 0.03 3.66 \pm 0.03	2.39 \pm 0.01 1.79 \pm 0.05	2.85 \pm 0.01 2.83 \pm 0.01	0.43 \pm 0.00 0.42 \pm 0.00	1.59 \pm 0.00 1.23 \pm 0.02 \uparrow 10.4%

340
 341 and test sets adhering to ratios of 8:1:1, a common split setting used in previous works (Zhang et al.,
 342 2021; Luo et al., 2025).

344 5.1.2 BASELINES

345 We perform the comparisons also using code pipeline PyOmniTS (Li et al., 2025). Twenty-six base-
 346 lines are included in the benchmark, covering SOTA methods categorized as (1) Multi-scale methods
 347 for IMTS: HD-TTS (Marisca et al., 2024), Hi-Patch (Luo et al., 2025), Warpformer (Zhang et al.,
 348 2023a), (2) Other SOTA methods for IMTS: TimeCHEAT (Liu et al., 2025), GNeuralFlow (Mercatali
 349 et al., 2024), tPatchGNN (Zhang et al., 2024), GraFITi (Yalavarthi et al., 2024), PrimeNet (Chowdhury
 350 et al., 2023), CRU (Schirmer et al., 2022), Raindrop (Zhang et al., 2021), NeuralFlows (Biloš et al.,
 351 2021), mTAN (Shukla & Marlin, 2020), SeFT (Horn et al., 2020), GRU-D (Che et al., 2018) (3) Multi-
 352 scale methods for regularly sampled time series: Ada-MSHyper (Shang et al., 2024), MOIRAI (Woo
 353 et al., 2024), TimeMixer (Wang et al., 2023), Pathformer (Chen et al., 2023), Scaleformer (Shabani
 354 et al., 2022), (4) Other SOTA methods for regularly sampled time series: Leddam (Yu et al., 2024),
 355 PatchTST (Nie et al., 2022), TimesNet (Wu et al., 2022), Crossformer (Zhang & Yan, 2022), Auto-
 356 former (Wu et al., 2021). We adapt their publicly available codes into the pipeline for comparisons,
 357 where network structures remain unchanged.

359 5.1.3 IMPLEMENTATION DETAILS

360 We follow the setting of widely acknowledged Time-Series-Library (Wang et al., 2024) in learning
 361 rate adjustments. All experiments run with a maximum of 300 epochs and early stopping patience
 362 of 10 epochs. To mitigate randomness, we conduct each experiment with five different random
 363 seeds ranging from 2024 to 2028 also following Time-Series-Library, calculating both the mean
 364 and standard deviation of the results. MSE is used as the training loss function for models, unless
 365 a custom loss function proposed in the original paper is used. When adapting regular time series
 366 models for IMTS, masks indicating observed values are included in the MSE calculations during
 367 training. The detailed settings for the hyperparameters are provided in Appendix E. Due to our more
 368 fine-grained hyperparameter searches for each experimental settings, baselines can perform better
 369 than those reported in previous works (Li et al., 2025; Yalavarthi et al., 2024; Zhang et al., 2024). All
 370 models are trained on a Linux server with PyTorch version 2.7.0 and two NVIDIA GeForce RTX
 371 3090 GPUs, while the efficiency analysis is conducted on another Linux server with PyTorch version
 372 2.2.2+cu118 and one NVIDIA GeForce RTX 2080Ti GPU.

373 5.2 MAIN RESULTS

374 Table 2 compares the ReIMTS version of existing IMTS models with respective baselines, and
 375 Table 3 shows the models’ forecasting performance. Both are evaluated using MSE across five
 376 datasets, with the best results highlighted in bold. The visualization of forecasting results can be

378
 379 Table 3: Experimental results for other state-of-the-art regular and irregular baselines on five irregular
 380 multivariate time series datasets evaluated by MSE (mean \pm std) $\times 10^{-1}$. The best and second-best
 381 results are indicated in **bold** and underlined, respectively. ‘ME’ indicates memory error.
 382

	Algorithm	MIMIC-III	MIMIC-IV	PhysioNet’12	Human Activity	USHCN
Regular	MOIRAI	8.66 \pm 0.00	4.29 \pm 0.00	4.92 \pm 0.00	1.08 \pm 0.00	12.32 \pm 0.00
	Ada-MSHyper	6.16 \pm 0.01	3.89 \pm 0.01	4.06 \pm 0.02	1.48 \pm 0.04	2.41 \pm 0.19
	Autoformer	7.08 \pm 0.08	5.45 \pm 0.16	4.14 \pm 0.04	0.98 \pm 0.07	4.37 \pm 0.45
	Scaleformer	5.50 \pm 0.07	4.55 \pm 0.13	4.02 \pm 0.02	1.01 \pm 0.05	5.50 \pm 0.73
	TimesNet	5.78 \pm 0.01	3.82 \pm 0.01	4.08 \pm 0.01	1.21 \pm 0.03	2.40 \pm 0.12
	NHITS	5.83 \pm 0.01	3.95 \pm 0.01	3.84 \pm 0.01	0.98 \pm 0.01	2.71 \pm 0.09
	Pyraformer	5.69 \pm 0.02	4.08 \pm 0.04	3.82 \pm 0.00	1.17 \pm 0.01	2.35 \pm 0.27
	PatchTST	5.68 \pm 0.01	2.94 \pm 0.01	3.40 \pm 0.01	0.68 \pm 0.00	2.83 \pm 0.75
	Leddam	5.93 \pm 0.00	3.70 \pm 0.02	3.75 \pm 0.03	0.91 \pm 0.01	2.89 \pm 0.26
	Pathformer	5.59 \pm 0.13	ME	3.46 \pm 0.01	0.91 \pm 0.01	2.98 \pm 0.40
Irregular	Crossformer	5.37 \pm 0.01	3.00 \pm 0.02	3.39 \pm 0.05	1.41 \pm 0.21	2.12 \pm 0.04
	TimeMixer	5.67 \pm 0.05	3.54 \pm 0.02	3.25 \pm 0.01	0.67 \pm 0.02	2.45 \pm 0.10
	SeFT	9.23 \pm 0.01	6.60 \pm 0.00	7.67 \pm 0.01	13.76 \pm 0.02	3.34 \pm 0.01
	NeuralFlows	7.17 \pm 0.03	4.74 \pm 0.02	4.20 \pm 0.02	1.68 \pm 0.03	2.01 \pm 0.04
	CRU	7.07 \pm 0.03	4.35 \pm 0.02	6.19 \pm 0.01	1.37 \pm 0.04	2.26 \pm 0.09
	GNeuralFlow	6.95 \pm 0.05	5.01 \pm 0.02	3.88 \pm 0.03	1.73 \pm 0.01	1.83 \pm 0.03
	tPatchGNN	5.17 \pm 0.04	2.74 \pm 0.02	3.22 \pm 0.02	0.44 \pm 0.01	1.82 \pm 0.18
	Hi-Patch	4.35 \pm 0.02	2.36 \pm 0.02	3.11 \pm 0.05	0.48 \pm 0.01	1.60 \pm 0.08
	Warpformer	4.09 \pm 0.01	2.42 \pm 0.02	2.88 \pm 0.01	0.54 \pm 0.01	1.56 \pm 0.01
	HD-TTS	4.17 \pm 0.01	2.36 \pm 0.00	2.83 \pm 0.01	0.50 \pm 0.01	1.66 \pm 0.05
ReIMTS (Ours)		3.66 \pm 0.03	1.79 \pm 0.05	2.83 \pm 0.01	0.42 \pm 0.00	1.23 \pm 0.02

402
 403 found in Appendix D. The lookback time periods are 36 hours for MIMIC-III, MIMIC-VI, and
 404 PhysioNet’12, 3000 milliseconds for Human Activity, and 3 years for USHCN. Human Activity uses
 405 a forecast length of 300 milliseconds, and the rest datasets use the next 3 timestamps as forecast
 406 targets, following the settings in existing works (Biloš et al., 2021; De Brouwer et al., 2019). Results
 407 evaluated using MAE are detailed in Appendix B.3, and an analysis of varying forecast horizons
 408 can be found in Appendix B.4. As can be seen, our method ReIMTS boosts the performance of six
 409 existing IMTS models by an average of 29.1%, including well-known models and SOTA ones. When
 410 using GraFITi as the backbone, ReIMTS achieves the best performance compared to all baseline
 411 models. Compared to existing multi-scale methods for IMTS such as Hi-Patch, Warpformer, and
 412 HD-TTS, ReIMTS demonstrates superior extensibility by integrating multi-scale techniques without
 413 requiring a dedicated multi-scale module within the backbone. We also observe that older methods,
 414 such as mTAN and GRU-D, can also achieve performance improvements and even outperform more
 415 recent models. This demonstrates the potential of enhancing classic methods for IMTS forecasting
 416 with our approach. PrimeNet demonstrates significant performance improvements after applying
 417 ReIMTS, which may suggest that its pretraining-finetuning approach require more input samples to
 418 achieve optimal performance, and we further discuss it in Appendix B.4. As for regularly sampled
 419 time series models, some of them can surpass relatively old IMTS models, which shows the necessity
 420 of comprehensive comparisons.

421 Table 4: Ablation results of ReIMTS and its four variants on five irregular multivariate time series
 422 datasets using GraFITi as the backbone.
 423

Ablation	MIMIC-III	MIMIC-IV	PhysioNet’12	Human Activity	USHCN
ReIMTS	3.66 \pm 0.03	1.79 \pm 0.05	2.83 \pm 0.01	0.42 \pm 0.00	1.23 \pm 0.02
rp sample	4.86 \pm 0.02	1.92 \pm 0.04	2.83 \pm 0.01	0.45 \pm 0.01	1.23 \pm 0.03
rp split	5.06 \pm 0.04	2.36 \pm 0.03	3.20 \pm 0.01	0.61 \pm 0.02	1.30 \pm 0.10
rp IARF	5.07 \pm 0.22	1.84 \pm 0.02	2.79 \pm 0.00	0.47 \pm 0.01	1.23 \pm 0.03
w/o IARF	4.98 \pm 0.07	2.07 \pm 0.04	3.06 \pm 0.00	0.54 \pm 0.00	1.36 \pm 0.01

432 5.3 EFFICIENCY ANALYSIS
433

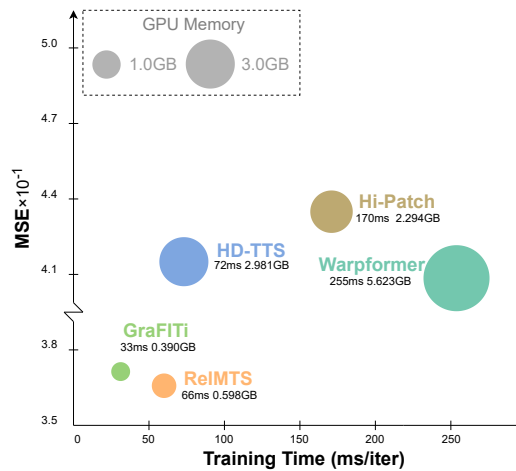
434 We compare the efficiency of our method
435 ReIMTS with existing multi-scale methods
436 for IMTS, namely Warpformer (Zhang et al.,
437 2023a), HD-TTS (Marisca et al., 2024), and Hi-
438 Patch (Luo et al., 2025). GraFITi (Yalavarthi
439 et al., 2024) is used as the backbone in ReIMTS,
440 and we also perform a comparison with it. Mod-
441 els are assessed based on their MSE, training
442 time, and GPU memory footprint. The training
443 time for one epoch with a batch size of
444 32 is recorded, then divided by the number of
445 batches to determine the training time per iter-
446 ation. Memory footprints only encompass the
447 model’s usage instead of representing the entire
448 process. Results on the MIMIC-III dataset are
449 shown in Figure 4, and results from the remain-
450 ing datasets are plotted in Figure 6 and discussed
451 in Appendix B.5. As can be seen, ReIMTS runs
452 the fastest and uses the least GPU memory com-
453 pared to existing multi-scale methods for IMTS,
454 while achieving the lowest MSE. It demon-
455 strates ReIMTS’s flexibility in using lightweight
456 backbones and scalability in performing the best.
457 Compared with the original backbone GraFITi,
458 ReIMTS controls the overhead of multi-scale
459 learning within an acceptable range, without the
460 GPU memory usage being proportional to the number
461 of scale levels.

462 5.4 ABLATION STUDY

463 We evaluate the performance of ReIMTS and its four variants across all five datasets. (1) **rp sample**
464 replaces split subsamples with original sample; (2) **rp split** splits subsamples based on the number of
465 observations rather than time periods; (3) **rp IARF** replaces irregularity-aware representation fusion
466 with addition; (4) **w/o IARF** removes irregularity-aware representation fusion; The ablation results
467 are summarized in Table 4. As can be seen, all model designs are necessary. Results from **rp sample**
468 and **rp split** show the necessity of splitting samples, particularly by time periods rather than the
469 number of observations. **rp IARF** and **w/o IARF** demonstrate the effectiveness of irregularity-aware
470 representation fusion, and highlight the necessity of leveraging both global and local representations.

471 6 CONCLUSION

472 This paper introduces a recursive multi-scale method, ReIMTS, to address the IMTS forecasting
473 problem. ReIMTS recursively divides original IMTS samples into subsamples with shorter time
474 periods while maintaining the original sampling patterns. By recursively invoking the backbone to
475 learn representations at each scale level, ReIMTS retrieves global-to-local multi-scale representa-
476 tions based on the preserved sampling patterns. Moreover, ReIMTS leverages an irregularity-aware
477 representation fusion mechanism to adaptively combine global and local representations based on
478 content and sampling patterns, thereby preserving crucial semantics for accurate forecasting. ReIMTS
479 exhibits strong flexibility and improves performance across various existing IMTS backbones, out-
480 performing twenty-six baseline models in our unified code pipeline. Nevertheless, ReIMTS still has
481 more potential in combining with wider range of backbones. ODE-based models might need further
482 theoretical explainability when used with our method. Additionally, some diffusion-based models
483 predict noisy latent representations in their backbones, which may not be directly compatible with
484 our method. Possible solutions include predicting clean observations during the denoising process, or
485 using ReIMTS within the denoising backbone. We will investigate these challenges further in future
work.



477 Figure 4: Model efficiency comparison on MIMIC-
478 III, with a 36-hour lookback length, 3 forecast
479 timestamps, 96 variables, and a batch size of 32.
480 ReIMTS uses GraFITi as backbone in the figure,
481 which achieves the best efficiency compared to
482 other multi-scale IMTS methods, including Warp-
483 former, HD-TTS, and Hi-Patch.

486 REFERENCES
487

488 Mansour Almazroui, M. Nazrul Islam, H. Athar, P. D. Jones, and M. Ashfaqur Rahman. Recent
489 climate change in the Arabian Peninsula: Annual rainfall and temperature analysis of Saudi Arabia
490 for 1978–2009. *International Journal of Climatology*, 32(6):953–966, 2012. ISSN 1097-0088.
491 doi: 10.1002/joc.3446.

492 Marin Biloš, Johanna Sommer, Syama Sundar Rangapuram, Tim Januschowski, and Stephan
493 Günnemann. Neural Flows: Efficient Alternative to Neural ODEs. In *Advances in Neural
494 Information Processing Systems*, volume 34, pp. 21325–21337. Curran Associates, Inc., 2021.

495 Cristian Challu, Kin G. Olivares, Boris N. Oreshkin, Federico Garza Ramirez, Max Mergenthaler
496 Canseco, and Artur Dubrawski. NHITS: Neural Hierarchical Interpolation for Time Series
497 Forecasting. *Proceedings of the AAAI Conference on Artificial Intelligence*, 37(6):6989–6997,
498 2023. ISSN 2374-3468. doi: 10.1609/aaai.v37i6.25854.

499 Zhengping Che, Sanjay Purushotham, Kyunghyun Cho, David Sontag, and Yan Liu. Recurrent
500 Neural Networks for Multivariate Time Series with Missing Values. *Scientific Reports*, 8(1):6085,
501 2018. ISSN 2045-2322. doi: 10.1038/s41598-018-24271-9.

502 Peng Chen, Yingying Zhang, Yunyao Cheng, Yang Shu, Yihang Wang, Qingsong Wen, Bin Yang, and
503 Chenjuan Guo. Pathformer: Multi-scale Transformers with Adaptive Pathways for Time Series
504 Forecasting. In *The Twelfth International Conference on Learning Representations*, 2023.

505 Zipeng Chen, Qianli Ma, and Zhenxi Lin. Time-Aware Multi-Scale RNNs for Time Series Modeling.
506 In *Twenty-Ninth International Joint Conference on Artificial Intelligence*, volume 3, pp. 2285–2291,
507 2021. doi: 10.24963/ijcai.2021/315.

508 Ranak Roy Chowdhury, Jiacheng Li, Xiyuan Zhang, Dezhi Hong, Rajesh K. Gupta, and Jingbo
509 Shang. PrimeNet: Pre-training for Irregular Multivariate Time Series. *Proceedings of the AAAI
510 Conference on Artificial Intelligence*, 37(6):7184–7192, 2023. ISSN 2374-3468. doi: 10.1609/aaai.
511 v37i6.25876.

512 Edward De Brouwer, Jaak Simm, Adam Arany, and Yves Moreau. GRU-ODE-Bayes: Continuous
513 Modeling of Sporadically-Observed Time Series. In *Advances in Neural Information Processing
514 Systems*, volume 32. Curran Associates, Inc., 2019.

515 Nick Holford. Treatment response and disease progression. *Translational and Clinical Pharmacology*,
516 27(4):123–126, 2019. ISSN 2289-0882. doi: 10.12793/tcp.2019.27.4.123.

517 Max Horn, Michael Moor, Christian Bock, Bastian Rieck, and Karsten Borgwardt. Set Functions for
518 Time Series. In *International Conference on Machine Learning*, pp. 4353–4363. PMLR, 2020.

519 Alistair E. W. Johnson, Tom J. Pollard, Lu Shen, Li-wei H. Lehman, Mengling Feng, Mohammad
520 Ghassemi, Benjamin Moody, Peter Szolovits, Leo Anthony Celi, and Roger G. Mark. MIMIC-III,
521 a freely accessible critical care database. *Scientific Data*, 3(1):160035, 2016. ISSN 2052-4463.
522 doi: 10.1038/sdata.2016.35.

523 Alistair E. W. Johnson, Lucas Bulgarelli, Lu Shen, Alvin Gayles, Ayad Shammout, Steven Horng,
524 Tom J. Pollard, Sicheng Hao, Benjamin Moody, Brian Gow, Li-wei H. Lehman, Leo A. Celi, and
525 Roger G. Mark. MIMIC-IV, a freely accessible electronic health record dataset. *Scientific Data*,
526 10(1):1, 2023. ISSN 2052-4463. doi: 10.1038/s41597-022-01899-x.

527 Elizabeth B. Klerman, Allison Brager, Mary A. Carskadon, Christopher M. Depner, Russell Foster,
528 Namni Goel, Mary Harrington, Paul M. Holloway, Melissa P. Knauert, Monique K. LeBourgeois,
529 Jonathan Lipton, Martha Merrow, Sara Montagnese, Mingming Ning, David Ray, Frank A. J. L.
530 Scheer, Steven A. Shea, Debra J. Skene, Claudia Spies, Bart Staels, Marie-Pierre St-Onge, Steffen
531 Tiedt, Phyllis C. Zee, and Helen J. Burgess. Keeping an eye on circadian time in clinical research
532 and medicine. *Clinical and Translational Medicine*, 12(12):e1131, 2022. ISSN 2001-1326. doi:
533 10.1002/ctm2.1131.

534 Pavithra Lakshman, Priyanka T. Gopal, and Sheen Khurdi. Effectiveness of Remote Patient Moni-
535 toring Equipped With an Early Warning System in Tertiary Care Hospital Wards: Retrospective
536 Cohort Study. *Journal of Medical Internet Research*, 27(1):e56463, 2025. doi: 10.2196/56463.

540 Boyuan Li, Yicheng Luo, Zhen Liu, Junhao Zheng, Jianming Lv, and Qianli Ma. HyperIMTS:
 541 Hypergraph Neural Network for Irregular Multivariate Time Series Forecasting. In *Forty-Second*
 542 *International Conference on Machine Learning*, 2025.

543

544 Jixi Liu, Meng Cao, and Songcan Chen. TimeCHEAT: A Channel Harmony Strategy for Irregularly
 545 Sampled Multivariate Time Series Analysis. *Proceedings of the AAAI Conference on Artificial*
 546 *Intelligence*, 39(18):18861–18869, 2025. ISSN 2374-3468. doi: 10.1609/aaai.v39i18.34076.

547 Shizhan Liu, Hang Yu, Cong Liao, Jianguo Li, Weiyao Lin, Alex X. Liu, and Schahram Dustdar.
 548 Pyraformer: Low-Complexity Pyramidal Attention for Long-Range Time Series Modeling and
 549 Forecasting. In *International Conference on Learning Representations*, 2021.

550

551 Yicheng Luo, Zhen Liu, Linghao Wang, Binquan Wu, Junhao Zheng, and Qianli Ma. Knowledge-
 552 Empowered Dynamic Graph Network for Irregularly Sampled Medical Time Series. In *The*
 553 *Thirty-eighth Annual Conference on Neural Information Processing Systems*, 2024.

554 Yicheng Luo, Bowen Zhang, Zhen Liu, and Qianli Ma. Hi-Patch: Hierarchical Patch GNN for
 555 Irregular Multivariate Time Series. In *Forty-Second International Conference on Machine Learning*,
 556 2025.

557

558 Ivan Marisca, Cesare Alippi, and Filippo Maria Bianchi. Graph-based Forecasting with Missing Data
 559 through Spatiotemporal Downsampling. In *International Conference on Machine Learning*, pp.
 560 34846–34865. PMLR, 2024.

561 M.J. Menne, C.N. Williams, Jr., and R.S. Vose. Long-term daily and monthly climate records from
 562 stations across the contiguous united states (u.s. historical climatology network). 1 2016. doi:
 563 10.3334/CDIAC/CLI.NDP019.

564

565 Giangiocomo Mercatali, Andre Freitas, and Jie Chen. Graph Neural Flows for Unveiling Systemic
 566 Interactions Among Irregularly Sampled Time Series. In *The Thirty-eighth Annual Conference on*
 567 *Neural Information Processing Systems*, 2024.

568 Wayne L. Miller, Karen A. Hartman, Mary F. Burritt, Diane E. Grill, Richard J. Rodeheffer, John C.
 569 Burnett, and Allan S. Jaffe. Serial Biomarker Measurements in Ambulatory Patients With Chronic
 570 Heart Failure. *Circulation*, 116(3):249–257, 2007. doi: 10.1161/CIRCULATIONAHA.107.
 571 694562.

572

573 James H. Morrill, Andrey Kormilitzin, Alejo J. Nevado-Holgado, Sumanth Swaminathan, Samuel D.
 574 Howison, and Terry J. Lyons. Utilization of the Signature Method to Identify the Early Onset of
 575 Sepsis From Multivariate Physiological Time Series in Critical Care Monitoring. *Critical Care*
 576 *Medicine*, 48(10):e976, 2020. ISSN 1530-0293. doi: 10.1097/CCM.0000000000004510.

577 Yuqi Nie, Nam H. Nguyen, Phanwadee Sinthong, and Jayant Kalagnanam. A Time Series is Worth
 578 64 Words: Long-term Forecasting with Transformers. In *The Eleventh International Conference*
 579 *on Learning Representations*, 2022.

580 Attila Reiss and Didier Stricker. Introducing a New Benchmarked Dataset for Activity Monitoring. In
 581 *2012 16th Annual International Symposium on Wearable Computers (ISWC)*, pp. 108–109. IEEE,
 582 2012. ISBN 978-0-7695-4697-1 978-1-4673-1583-8. doi: 10.1109/ISWC.2012.13.

583

584 Yulia Rubanova, Ricky T. Q. Chen, and David K Duvenaud. Latent Ordinary Differential Equations
 585 for Irregularly-Sampled Time Series. In *Advances in Neural Information Processing Systems*,
 586 volume 32. Curran Associates, Inc., 2019.

587

588 Mona Schirmer, Mazin Eltayeb, Stefan Lessmann, and Maja Rudolph. Modeling Irregular Time
 589 Series with Continuous Recurrent Units. In *International Conference on Machine Learning*, pp.
 590 19388–19405. PMLR, 2022.

591 Seymour Christopher W., Gesten Foster, Prescott Hallie C., Friedrich Marcus E., Iwashyna Theodore
 592 J., Phillips Gary S., Lemeshow Stanley, Osborn Tiffany, Terry Kathleen M., and Levy Mitchell
 593 M. Time to Treatment and Mortality during Mandated Emergency Care for Sepsis. *New England*
Journal of Medicine, 376(23):2235–2244, 2017. doi: 10.1056/NEJMoa1703058.

594 Mohammad Amin Shabani, Amir H. Abdi, Lili Meng, and Tristan Sylvain. Scaleformer: Iterative
 595 Multi-scale Refining Transformers for Time Series Forecasting. In *The Eleventh International*
 596 *Conference on Learning Representations*, 2022.

597

598 Zongjiang Shang, Ling Chen, Binqing Wu, and Dongliang Cui. Ada-MSHyper: Adaptive Multi-Scale
 599 Hypergraph Transformer for Time Series Forecasting. In *The Thirty-eighth Annual Conference on*
 600 *Neural Information Processing Systems*, 2024.

601

602 Satya Narayan Shukla and Benjamin Marlin. Interpolation-Prediction Networks for Irregularly
 603 Sampled Time Series. In *International Conference on Learning Representations*, 2018.

604

605 Satya Narayan Shukla and Benjamin Marlin. Multi-Time Attention Networks for Irregularly Sampled
 606 Time Series. In *International Conference on Learning Representations*, 2020.

607

608 Satya Narayan Shukla and Benjamin M. Marlin. A Survey on Principles, Models and Methods for
 609 Learning from Irregularly Sampled Time Series. *arXiv preprint*, 2021. doi: 10.48550/arXiv.2012.
 00168.

610

611 Ikaro Silva, George Moody, Daniel J Scott, Leo A Celi, and Roger G Mark. Predicting In-Hospital
 612 Mortality of ICU Patients: The PhysioNet/Computing in Cardiology Challenge 2012. *Computing*
 613 in *cardiology*, 39:245–248, 2012.

614

615 Yusuke Tashiro, Jiaming Song, Yang Song, and Stefano Ermon. CSDI: Conditional Score-based
 616 Diffusion Models for Probabilistic Time Series Imputation. In *Advances in Neural Information*
 617 *Processing Systems*, volume 34, pp. 24804–24816. Curran Associates, Inc., 2021.

618

619 Shiyu Wang, Haixu Wu, Xiaoming Shi, Tengge Hu, Huakun Luo, Lintao Ma, James Y. Zhang, and
 620 Jun Zhou. TimeMixer: Decomposable Multiscale Mixing for Time Series Forecasting. In *The*
 621 *Twelfth International Conference on Learning Representations*, 2023.

622

623 Yuxuan Wang, Haixu Wu, Jiaxiang Dong, Yong Liu, Mingsheng Long, and Jianmin Wang. Deep
 624 Time Series Models: A Comprehensive Survey and Benchmark. *arXiv preprint*, 2024. doi:
 10.48550/arXiv.2407.13278.

625

626 Gerald Woo, Chenghao Liu, Akshat Kumar, Caiming Xiong, Silvio Savarese, and Doyen Sahoo.
 627 Unified Training of Universal Time Series Forecasting Transformers. In *International Conference*
 628 *on Machine Learning*, pp. 53140–53164. PMLR, 2024.

629

630 Haixu Wu, Jiehui Xu, Jianmin Wang, and Mingsheng Long. Autoformer: Decomposition Transfor-
 631 *mers with Auto-Correlation for Long-Term Series Forecasting*. In *Advances in Neural Information*
 632 *Processing Systems*, volume 34, pp. 22419–22430. Curran Associates, Inc., 2021.

633

634 Haixu Wu, Tengge Hu, Yong Liu, Hang Zhou, Jianmin Wang, and Mingsheng Long. TimesNet:
 635 Temporal 2D-Variation Modeling for General Time Series Analysis. In *The Eleventh International*
 636 *Conference on Learning Representations*, 2022.

637

638 Vijaya Krishna Yalavarthi, Kiran Madhusudhanan, Randolph Scholz, Nourhan Ahmed, Johannes
 639 Burchert, Shayan Jawed, Stefan Born, and Lars Schmidt-Thieme. GraFITi: Graphs for Forecasting
 Irregularly Sampled Time Series. *Proceedings of the AAAI Conference on Artificial Intelligence*,
 38(15):16255–16263, 2024. ISSN 2374-3468. doi: 10.1609/aaai.v38i15.29560.

640

641 Guoqi Yu, Jing Zou, Xiaowei Hu, Angelica I. Aviles-Rivero, Jing Qin, and Shujun Wang. Revitalizing
 642 Multivariate Time Series Forecasting: Learnable Decomposition with Inter-Series Dependencies
 643 and Intra-Series Variations Modeling. In *Forty-First International Conference on Machine Learn-
 644 ing*, 2024.

645

646 Jiawen Zhang, Shun Zheng, Wei Cao, Jiang Bian, and Jia Li. Warpformer: A Multi-scale Modeling
 647 Approach for Irregular Clinical Time Series. In *Proceedings of the 29th ACM SIGKDD Conference*
 648 *on Knowledge Discovery and Data Mining*, pp. 3273–3285, 2023a. doi: 10.1145/3580305.
 3599543.

648 Kexin Zhang, Qingsong Wen, Chaoli Zhang, Rongyao Cai, Ming Jin, Yong Liu, James Zhang,
649 Yuxuan Liang, Guansong Pang, Dongjin Song, and Shirui Pan. Self-Supervised Learning for Time
650 Series Analysis: Taxonomy, Progress, and Prospects. *arXiv preprint*, 2023b. doi: 10.48550/arXiv.
651 2306.10125.

652 Weijia Zhang, Chenlong Yin, Hao Liu, Xiaofang Zhou, and Hui Xiong. Irregular Multivariate Time
653 Series Forecasting: A Transformable Patching Graph Neural Networks Approach. In *Forty-First*
654 *International Conference on Machine Learning*, 2024.

655 Xiang Zhang, Marko Zeman, Theodoros Tsiligkaridis, and Marinka Zitnik. Graph-Guided Network
656 for Irregularly Sampled Multivariate Time Series. In *International Conference on Learning*
657 *Representations*, 2021.

658 Yunhao Zhang and Junchi Yan. Crossformer: Transformer Utilizing Cross-Dimension Dependency
659 for Multivariate Time Series Forecasting. In *The Eleventh International Conference on Learning*
660 *Representations*, 2022.

661

662

663

664

665

666

667

668

669

670

671

672

673

674

675

676

677

678

679

680

681

682

683

684

685

686

687

688

689

690

691

692

693

694

695

696

697

698

699

700

701

702 **Algorithm 1** ReIMTS: Learning Recursive Multi-Scale Representations

703

704 **Require:** input IMTS $\mathbf{S}^1 \in \mathbb{R}^{L^1 \times V}$, binary mask $\mathbf{M}^1 \in \{0, 1\}^{L^1 \times V}$, scale level $n \in \{1, \dots, N\}$,
705 a series of time periods $\{T^n\}_{n=1}^N$, forecast horizon L_Q ,
706 IMTS backbone decoder \mathcal{F}_{dec} , and a series of encoders in IMTS backbones $\{\mathcal{F}_{\text{enc}}^n\}_{n=1}^N$.

707 **Ensure:** forecast result $\hat{\mathbf{Z}} \in \mathbb{R}^{L_Q \times V}$

708 **function** REIMTS($\mathbf{S}^n, \mathbf{M}^n, n, N, \{T^n\}_{n=1}^N, L_Q, \{\mathcal{F}_{\text{enc}}^n\}_{n=1}^N, \mathcal{F}_{\text{dec}}, \mathbf{H}^{n-1}$)
709 $\mathbf{E}^n \leftarrow \mathcal{F}_{\text{enc}}^n(\mathbf{S}^n, L_Q)$ ▷ Equation (3) of the paper
710 **if** $\mathbf{H}^{n-1} \neq \text{null}$ **then**
711 $\mathbf{G}^n = \text{Fuse}(\mathbf{E}^n, \mathbf{H}^{n-1}, \mathbf{M}^n)$ ▷ Equation (4), (5), and (6) of the paper
712 **else**
713 $\mathbf{G}^n = \mathbf{E}^n$
714 **end if**
715 **if** $n = N$ **then**
716 $\hat{\mathbf{Z}} \leftarrow \mathcal{F}_{\text{dec}}^n(\mathbf{G}^n, L_Q)$ ▷ Base case
717 **return** $\hat{\mathbf{Z}}$
718 **else**
719 $\mathbf{S}^{n+1} \leftarrow \text{Split}(\mathbf{S}^n, T^{n+1})$ ▷ Equation (2) of the paper
720 $\mathbf{M}^{n+1} \leftarrow \text{Split}(\mathbf{M}^n, T^{n+1})$
721 $\mathbf{H}^n \leftarrow \text{SplitOrDuplicate}(\mathbf{G}^n)$ ▷ Equation (9), (10), and (11) of the paper
722 REIMTS($\mathbf{S}^{n+1}, \mathbf{M}^{n+1}, n+1, N, \{T^n\}_{n=1}^N, L_Q, \{\mathcal{F}_{\text{enc}}^n\}_{n=1}^N, \mathcal{F}_{\text{dec}}, \mathbf{H}^n$) ▷ Recursive call
723 **end if**
724 **end function**
725 **procedure** MAIN
726 $\hat{\mathbf{Z}} \leftarrow \text{REIMTS}(\mathbf{S}^1, \mathbf{M}^1, 1, N, \{T^n\}_{n=1}^N, L_Q, \{\mathcal{F}_{\text{enc}}^n\}_{n=1}^N, \mathcal{F}_{\text{dec}}, \text{null})$
727 **return** $\hat{\mathbf{Z}}$
728 **end procedure**

A RECURSIVE REPRESENTATION SPLITTING OR DUPLICATION

730 After \mathbf{E}^n is fused with the representation from scale level $n-1$ to obtain \mathbf{G}^n as detailed in Section 4.2,
731 for the temporal representation case $\mathbf{G}_{\text{time}}^n := \{\mathbf{g}_{\text{time}}^n(\mathbf{t}_k^n)\}_{k=1}^{P^n}$ where $\mathbf{G}_{\text{time}}^n \in \mathbb{R}^{P^n \times L^n \times D}$, ReIMTS
732 splits them along the time dimension before passing these global representations to the lower $n+1$
733 scale level. It should be noted that in this discussion, ‘global’ and ‘local’ are used to describe relative
734 scales between upper and lower levels, rather than considering all N levels. The splitting process is
735 similar to that for original IMTS samples, with split positions determined by time periods:
736

$$\mathbf{H}_{\text{time}}^n := \{\mathbf{g}_{\text{time}}^n(\mathbf{t}_{k'}^{n+1})\}_{k'=1}^{P^{n+1}}, \quad (9)$$

737 where $\mathbf{H}_{\text{time}}^n \in \mathbb{R}^{P^{n+1} \times L^{n+1} \times D}$. It should be noted that although representations from different levels
738 share the same timestamps, the dependencies they learn differ. Global dependencies $\mathbf{H}_{\text{time}}^n$ are learned
739 from time periods of length T^n , while local ones $\mathbf{E}_{\text{time}}^{n+1}$ correspond to shorter time periods of length
740 T^{n+1} .

741 The observation representation case $\mathbf{G}_{\text{obs}}^n := \{\mathbf{g}_{\text{obs}}^n(\mathbf{t}_k^n)\}_{k=1}^{P^n}$, where $\mathbf{G}_{\text{obs}}^n \in \mathbb{R}^{P^n \times L^n \times V \times D}$, is
742 similar to the temporal representation case. We also split them using time periods:
743

$$\mathbf{H}_{\text{obs}}^n := \{\mathbf{g}_{\text{obs}}^n(\mathbf{t}_{k'}^{n+1})\}_{k'=1}^{P^{n+1}}, \quad (10)$$

744 where $\mathbf{H}_{\text{obs}}^n \in \mathbb{R}^{P^{n+1} \times L^{n+1} \times V \times D}$. As for the variable representation case $\mathbf{G}_{\text{var}}^n := \{\mathbf{g}_{\text{var}}^n(\mathbf{t}_k^n)\}_{k=1}^{P^n}$
745 where $\mathbf{G}_{\text{var}}^n \in \mathbb{R}^{P^n \times V \times D}$, we duplicate the number of representations P^n at scale level n for $\lceil \frac{P^{n+1}}{P^n} \rceil$
746 times, resulting in the same number of representations P^{n+1} at scale level $n+1$:

$$\mathbf{H}_{\text{var}}^n := \{\mathbf{g}_{\text{var}}^n(\mathbf{t}_{k'}^{n+1})\}_{k'=1}^{P^{n+1}}, \quad (11)$$

747 where $\mathbf{H}_{\text{var}}^n \in \mathbb{R}^{P^{n+1} \times V \times D}$.

756 **B ADDITIONAL EXPERIMENTS**
757758 **B.1 EFFECT OF SCALE LEVELS**
759760 Table 5: Effect of the number of scale levels on five datasets. A larger number of scale levels performs
761 better on datasets with longer maximum lengths and a sufficient number of samples.
762

Scale level	MIMIC-III	MIMIC-IV	PhysioNet'12	Human Activity	USHCN
2	3.66 ± 0.04	1.79 ± 0.05	2.86 ± 0.01	0.42 ± 0.00	1.23 ± 0.02
3	4.14 ± 0.02	1.95 ± 0.05	2.83 ± 0.01	0.71 ± 0.00	1.26 ± 0.02
4	3.98 ± 0.02	2.00 ± 0.02	2.84 ± 0.01	0.44 ± 0.00	1.40 ± 0.12

763
764 We assess how the number of scale levels impacts model performance, with results summarized
765 in Table 5. Time periods in different scale levels are 24h, 12h, and 6h for the healthcare datasets
766 MIMIC-III, MIMIC-IV, and PhysioNet'12, 2000ms, 1000ms, and 500ms for Human Activity, and
767 2 years, 1 year, and 6 months for USHCN. These chosen time periods are based on prior domain
768 knowledge, including cycles in clinical medicine (Lakshman et al., 2025; Holford, 2019; Morrill
769 et al., 2020) and periodic changes in climate (Almazroui et al., 2012). In general, most datasets
770 achieve optimal performance at a scale level of 2, except for PhysioNet'12. Although the USHCN
771 dataset has a relatively long maximum length, it suffers from an insufficient number of samples for
772 training a robust model, as reported in previous work (Yalavarthi et al., 2024).
773

774 **B.2 EFFECT OF TIME PERIODS**
775

776 The impact of varying time periods on model performance is demonstrated in Figure 5 for all datasets.
777 We fix the number of scale levels to two for these experiments. As can be seen, time periods
778 corresponding to optimal performance across all datasets are half the total time length when the
779 number of scale levels is two. This is expected given that most IMTS datasets are sparse, exhibiting
780 dependencies over long time periods, as discussed in Appendix B.1. Specifically, for the medical
781 datasets MIMIC-III, MIMIC-IV, and PhysioNet'12, a 24-hour time length corresponds to the daily
782 cycles of patients.
783

784 **B.3 DIFFERENT METRICS**
785

786 We present the results measured using MAE in Table 6, which follows the same experimental setup
787 as Table 3. As can be seen, ReIMTS still outperforms all twenty-six baselines across all five datasets.
788 Additionally, it consistently enhances the performance of existing IMTS models under all settings,
789 aligning with the findings from the MSE evaluations discussed in Section 5.2.
790

791 **B.4 VARYING FORECAST HORIZONS**
792

793 We also evaluate performance across different forecast horizons. We follow the same settings as
794 in existing work (Zhang et al., 2024) and keep the lookback length settings the same as in Table 3.
795 For MIMIC-III, MIMIC-IV, and PhysioNet'12, the forecast horizon is set to 12 hours. For Human
796 Activity, the forecast horizon is 1000 milliseconds. For USHCN, the forecast horizon is set to 1 year.
797 The results are summarized in Table 7. It is evident that ReIMTS consistently enhances performance
798 across longer forecast lengths. Regarding other baseline models, we have surprisingly noticed that a
799 few models can outperform others in forecasting longer time horizons, as the empirical results have
800 been thoroughly verified. For example, GRU-D exhibits lower MSE across all five datasets when
801 forecasting longer lengths, so as ReIMTS+GRU-D. This might due to the longer chains of hidden
802 states, where GRU-D views forecasting as a task of imputation on the right side of the input series.
803 Also, PrimeNet performs better on longer forecast lengths, suggesting that apart from requiring more
804 input samples, its pretraining-finetuning approach may also require more training targets in forecast
805 horizons to achieve optimal performance. It should be noted that, unlike fully observed MTS, IMTS
806 samples are typically split into lookback and forecast window based on time periods rather than the
807 number of observations. The forecast settings here view 75% of the time period as the lookback
808 window, while the remaining 25% as the forecast window.
809

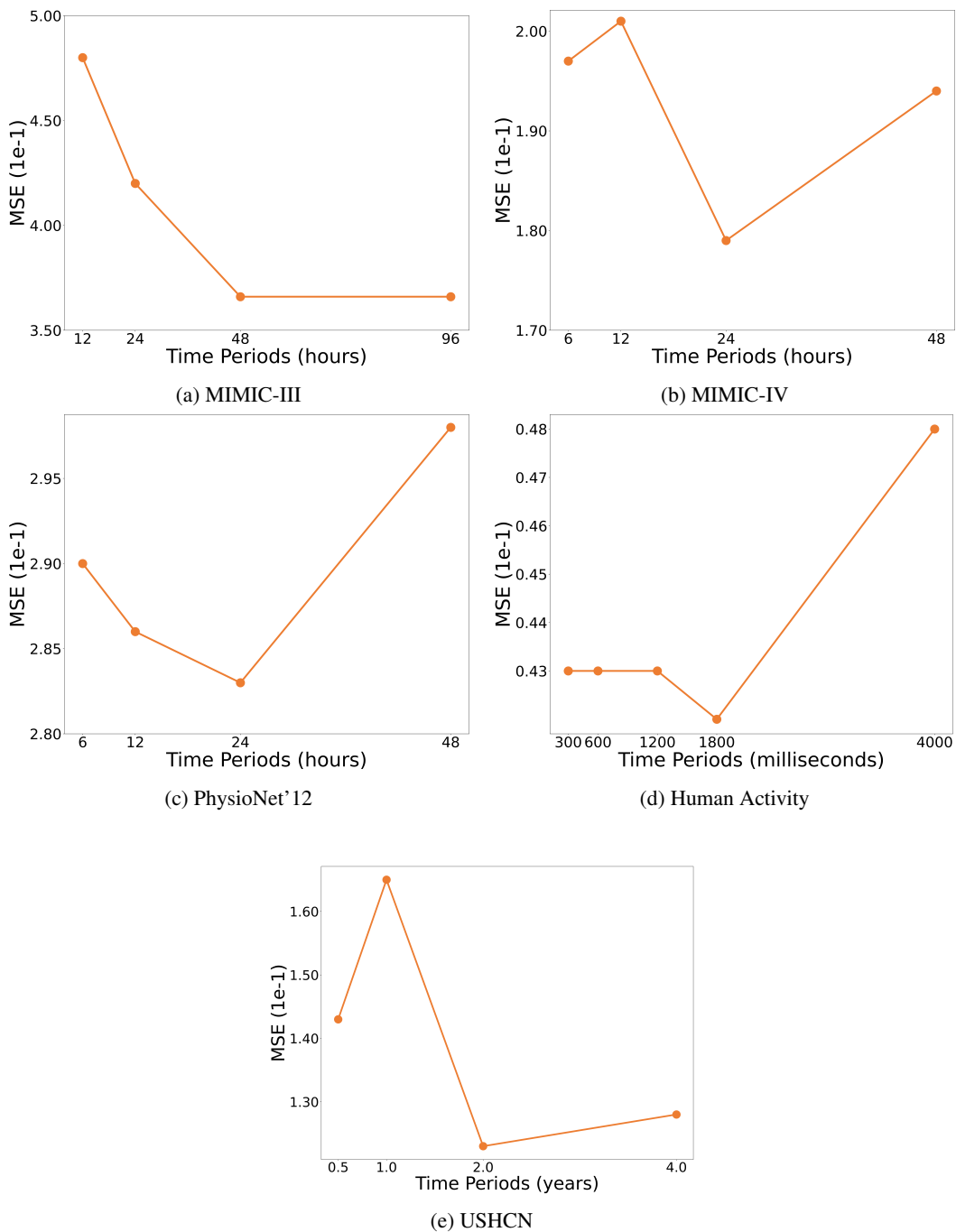


Figure 5: Effect of different time period lengths on PhysioNet'12, Human Activity, and USHCN.

864
865
866
867
868
869
870
871
872
873
874
875

876
877 Table 6: Experimental results on five irregular multivariate time series datasets, evaluated using MAE
878 (mean \pm std) $\times 10^{-1}$. The experimental setup is the same as in Table 3. ‘ME’ indicates Memory
879 Error.

880

	Algorithm	MIMIC-III	MIMIC-IV	PhysioNet’12	Human Activity	USHCN	Vs Ours
Regular	MOIRAI	5.79 \pm 0.00	4.00 \pm 0.00	4.94 \pm 0.00	1.91 \pm 0.00	8.27 \pm 0.00	
	Ada-MSHyper	5.22 \pm 0.00	4.28 \pm 0.01	4.50 \pm 0.00	2.61 \pm 0.04	3.19 \pm 0.07	
	Autoformer	5.47 \pm 0.03	5.20 \pm 0.00	4.53 \pm 0.03	2.18 \pm 0.06	4.10 \pm 0.05	
	Scaleformer	4.93 \pm 0.03	4.64 \pm 0.08	4.45 \pm 0.02	2.25 \pm 0.05	3.76 \pm 0.12	
	TimesNet	5.03 \pm 0.01	4.25 \pm 0.01	4.54 \pm 0.01	2.26 \pm 0.02	3.38 \pm 0.02	
	NHITS	4.92 \pm 0.01	4.13 \pm 0.01	4.29 \pm 0.01	2.16 \pm 0.01	3.42 \pm 0.04	
	Pyraformer	5.08 \pm 0.00	4.53 \pm 0.00	4.28 \pm 0.01	2.28 \pm 0.00	3.20 \pm 0.13	
	PatchTST	4.54 \pm 0.01	3.25 \pm 0.01	3.90 \pm 0.00	1.70 \pm 0.01	3.50 \pm 0.42	
	Leddam	4.83 \pm 0.03	3.98 \pm 0.02	4.28 \pm 0.02	2.00 \pm 0.01	3.13 \pm 0.07	
	Pathformer	4.75 \pm 0.02	ME	4.01 \pm 0.01	1.89 \pm 0.02	3.50 \pm 0.16	
Irregular	Crossformer	4.74 \pm 0.00	3.59 \pm 0.01	3.95 \pm 0.05	2.50 \pm 0.17	3.32 \pm 0.06	
	TimeMixer	4.75 \pm 0.04	3.88 \pm 0.02	3.80 \pm 0.01	1.66 \pm 0.03	3.13 \pm 0.06	
	PrimeNet	6.59 \pm 0.00	5.73 \pm 0.00	6.79 \pm 0.00	13.27 \pm 0.01	4.28 \pm 0.02	
	SeFT	6.62 \pm 0.00	5.88 \pm 0.01	6.68 \pm 0.01	9.75 \pm 0.01	4.08 \pm 0.04	
	mTAN	6.19 \pm 0.06	5.01 \pm 0.05	4.30 \pm 0.00	2.18 \pm 0.03	3.34 \pm 0.02	
	NeuralFlows	5.49 \pm 0.01	4.79 \pm 0.01	4.60 \pm 0.01	3.09 \pm 0.04	3.14 \pm 0.03	
	CRU	5.37 \pm 0.01	4.56 \pm 0.01	5.82 \pm 0.01	2.57 \pm 0.04	3.37 \pm 0.07	
	TimeCHEAT	4.12 \pm 0.03	2.97 \pm 0.01	3.70 \pm 0.00	1.70 \pm 0.06	3.78 \pm 0.18	
	GNeuralFlow	5.35 \pm 0.03	4.90 \pm 0.00	4.38 \pm 0.03	3.15 \pm 0.02	2.98 \pm 0.03	
	GRU-D	4.53 \pm 0.02	5.47 \pm 0.15	3.91 \pm 0.01	3.15 \pm 0.20	2.83 \pm 0.03	
ReIMTS	Raindrop	4.44 \pm 0.01	3.88 \pm 0.03	3.94 \pm 0.01	2.09 \pm 0.03	3.13 \pm 0.08	
	tPatchGNN	4.18 \pm 0.00	3.10 \pm 0.02	3.83 \pm 0.02	1.24 \pm 0.00	2.93 \pm 0.07	
	Hi-Patch	4.08 \pm 0.01	2.88 \pm 0.01	3.71 \pm 0.04	1.25 \pm 0.02	2.62 \pm 0.06	
	Warpformer	3.90 \pm 0.01	2.97 \pm 0.01	3.54 \pm 0.01	1.30 \pm 0.01	2.70 \pm 0.02	
	HD-TTS	3.94 \pm 0.00	2.94 \pm 0.01	3.49 \pm 0.01	1.39 \pm 0.04	2.94 \pm 0.12	
	GraFITi	3.69 \pm 0.02	3.07 \pm 0.02	3.52 \pm 0.01	1.20 \pm 0.00	2.75 \pm 0.13	
	+mTAN	5.17 \pm 0.03	4.23 \pm 0.05	3.96 \pm 0.01	2.11 \pm 0.01	2.42 \pm 0.03	↑13.9%
	+GRU-D	4.29 \pm 0.00	4.27 \pm 0.07	3.83 \pm 0.00	1.43 \pm 0.01	2.76 \pm 0.11	↑17.3%
	+Raindrop	4.40 \pm 0.02	3.64 \pm 0.05	3.76 \pm 0.01	1.97 \pm 0.01	2.62 \pm 0.08	↑5.6%
	+PrimeNet	4.34 \pm 0.00	4.04 \pm 0.01	3.64 \pm 0.02	2.02 \pm 0.00	2.53 \pm 0.04	↑47.1%
	+TimeCHEAT	4.10 \pm 0.04	2.56 \pm 0.06	3.51 \pm 0.01	1.47 \pm 0.01	2.51 \pm 0.11	↑13.3%
	+GraFITi	3.65 \pm 0.04	2.36 \pm 0.01	3.48 \pm 0.01	1.15 \pm 0.01	2.38 \pm 0.09	↑8.6%

906
907
908
909
910
911
912
913
914
915
916
917

918
 919 Table 7: Experimental results of varying forecast horizons on five irregular multivariate time series
 920 datasets evaluated using $\text{MSE} (\text{mean} \pm \text{std}) \times 10^{-1}$, with the lookback length following Table 3
 921 and forecast horizons set to the rest length of the whole series, which are 12 hours for MIMIC-III,
 922 MIMIC-IV, and PhysioNet'12, 1000 milliseconds for Human Activity, and 1 year for USHCN. ‘ME’
 923 indicates memory error.

	Algorithm	MIMIC-III	MIMIC-IV	PhysioNet'12	Human Activity	USHCN	Vs Ours
Regular	MOIRAI	9.68 ± 0.00	4.75 ± 0.00	5.36 ± 0.00	1.02 ± 0.00	8.94 ± 0.00	
	Ada-MSHyper	6.73 ± 0.05	4.30 ± 0.03	4.46 ± 0.02	1.60 ± 0.01	4.96 ± 0.04	
	Scaleformer	7.36 ± 0.08	4.84 ± 0.11	4.34 ± 0.03	1.54 ± 0.04	5.66 ± 0.09	
	NHITS	7.43 ± 0.02	5.16 ± 0.20	4.60 ± 0.01	1.10 ± 0.01	5.21 ± 0.09	
	Pyraformer	6.49 ± 0.02	4.71 ± 0.00	4.30 ± 0.01	1.23 ± 0.01	4.38 ± 0.04	
	PatchTST	5.90 ± 0.01	3.36 ± 0.00	3.91 ± 0.01	0.87 ± 0.01	4.78 ± 0.07	
	Pathformer	6.08 ± 0.10	ME	3.88 ± 0.01	0.91 ± 0.03	5.15 ± 0.08	
Irregular	TimeMixer	5.43 ± 0.02	3.71 ± 0.05	3.76 ± 0.01	0.69 ± 0.01	4.70 ± 0.01	
	PrimeNet	8.85 ± 0.00	5.90 ± 0.00	7.89 ± 0.00	10.94 ± 0.00	7.40 ± 0.00	
	mTAN	9.35 ± 0.32	4.95 ± 0.12	4.16 ± 0.02	1.01 ± 0.02	4.59 ± 0.03	
	TimeCHEAT	4.89 ± 0.03	3.02 ± 0.01	3.61 ± 0.30	0.74 ± 0.03	4.79 ± 0.15	
	GNeuralFlow	7.43 ± 0.07	4.83 ± 0.00	4.39 ± 0.02	1.89 ± 0.08	4.87 ± 0.05	
	GRU-D	5.53 ± 0.05	4.45 ± 0.00	3.81 ± 0.01	1.83 ± 0.23	5.32 ± 0.06	
	Raindrop	5.82 ± 0.02	5.58 ± 0.25	3.81 ± 0.01	0.97 ± 0.04	5.44 ± 0.41	
	tPatchGNN	5.90 ± 0.05	2.88 ± 0.00	3.81 ± 0.01	0.60 ± 0.01	5.44 ± 0.41	
	Hi-Patch	5.03 ± 0.02	2.97 ± 0.02	3.81 ± 0.00	0.59 ± 0.00	4.45 ± 0.10	
	Warpformer	4.83 ± 0.02	2.99 ± 0.00	3.62 ± 0.01	0.61 ± 0.01	4.46 ± 0.01	
	HD-TTS	5.62 ± 0.07	2.84 ± 0.02	3.78 ± 0.00	0.60 ± 0.01	4.56 ± 0.05	
	GraFITi	4.45 ± 0.04	2.72 ± 0.01	3.60 ± 0.01	0.60 ± 0.01	4.28 ± 0.09	
ReIMTS	+mTAN	6.54 ± 0.02	3.49 ± 0.01	3.94 ± 0.01	0.96 ± 0.01	4.48 ± 0.04	$\uparrow 14.4\%$
	+GRU-D	5.17 ± 0.05	3.85 ± 0.12	3.72 ± 0.05	1.39 ± 0.02	4.63 ± 0.09	$\uparrow 11.9\%$
	+Raindrop	5.52 ± 0.05	3.80 ± 0.02	3.74 ± 0.01	0.97 ± 0.01	4.98 ± 0.16	$\uparrow 9.5\%$
	+PrimeNet	5.17 ± 0.03	3.53 ± 0.01	3.67 ± 0.01	0.84 ± 0.01	4.42 ± 0.02	$\uparrow 53.6\%$
	+TimeCHEAT	4.75 ± 0.01	2.91 ± 0.02	3.55 ± 0.01	0.69 ± 0.04	4.39 ± 0.05	$\uparrow 4.7\%$
	+GraFITi	4.40 ± 0.02	2.50 ± 0.01	3.53 ± 0.01	0.55 ± 0.00	4.09 ± 0.18	$\uparrow 4.8\%$

B.5 ADDITIONAL EFFICIENCY ANALYSIS

We provide additional efficiency comparisons on datasets MIMIC-IV, PhysioNet'12, Human Activity, and USHCN, using the same settings as in Table 3. Results are summarized in Figure 6. ReIMTS uses GraFITi as its backbones in these comparisons. As can be seen, on most datasets, our method ReIMTS uses significantly fewer GPU memory than other multi-scale IMTS methods, including Warpformer, HD-TTS, and Hi-Patch. The training speed is similar to other multi-scale methods, while ReIMTS can achieve better performance. ReIMTS also has comparable efficiency with the original model GraFITi.

C BACKBONE DETAILS

We introduce how existing IMTS models serve as backbones in ReIMTS, with modifications potentially including reductions in hidden dimension size, layer count, or the removal of specific modules. Also, the structure of decoders and how backbones handle future timestamp queries and irregularities are also explained. We use the same strategy in the search of hyperparameters as compared baseline models, which aims to minimize the loss on validation sets. The number of layers is searched within 1, 2, 3, and 4, and the hidden dimension size is searched within 16, 32, 64, 128, 256, and 512. The number of scale levels used by ReIMTS are described in following paragraphs, which differs based on backbones. The time period lengths for all variants follow these settings: (1) MIMIC-III: 48 hours, 24 hours, 12 hours, and 6 hours; (2) MIMIC-IV: 48 hours, 24 hours, 12 hours, and 6 hours; (3) PhysioNet'12: 48 hours, 24 hours, 12 hours, and 6 hours; (4) Human Activity: 4000 milliseconds, 2000 milliseconds, 1000 milliseconds, and 500 milliseconds; (5) USHCN: 4 years, 2 years, 1 year, and 6 months. In the following descriptions, we use L_S and L_Q to denote the maximum number of observations in a univariate series in lookback and forecast window, respectively.

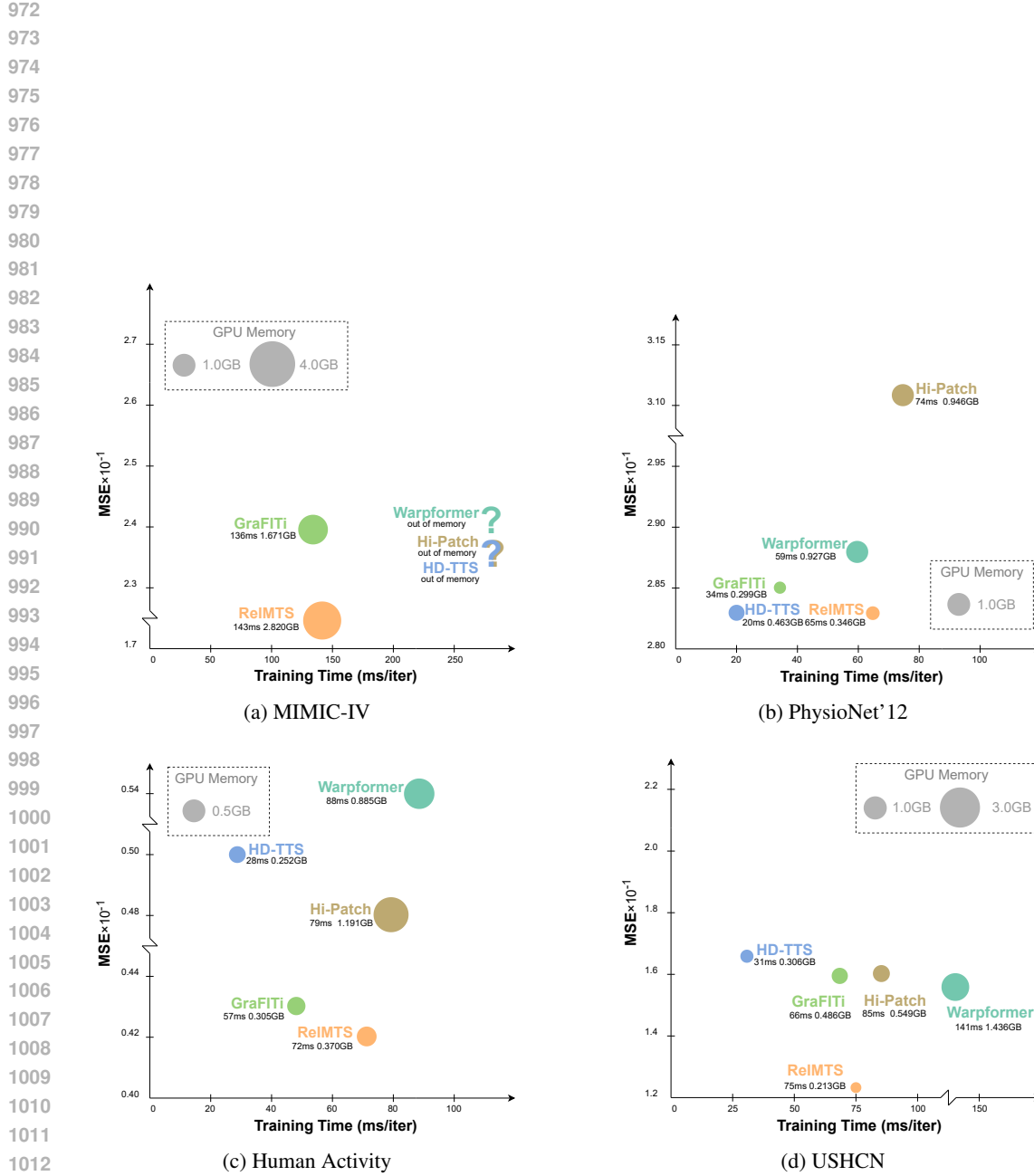


Figure 6: Efficiency comparisons on MIMIC-IV, PhysioNet'12, Human Activity, and USHCN with a batch size of 32. ReIMTS demonstrates significantly lower GPU memory usage than other multi-scale methods Warpformer, HD-TTS, and Hi-Patch on most datasets, while maintaining similar training time. Compared to the original backbone GraFITi, ReIMTS achieves comparable efficiency.

1026 **ReIMTS+mTAN** uses mTAN (Shukla & Marlin, 2020) as backbones. mTAN encodes input IMTS
 1027 into temporal representations at a fixed set of reference points, described in Figure 2(b) of its paper.
 1028 Therefore, it belongs to the case $\mathbf{E}^n = \mathbf{E}_{\text{time}}^n$ in Eq. 9, and we pass these temporal representations
 1029 from top to bottom within the ReIMTS architecture to learn multi-scale temporal representations. For
 1030 the decoder of mTAN, it consists of a GRU, a multi-head attention, and an MLP sequentially. It maps
 1031 temporal representations of shape $L_S \times D$ into time series $L_Q \times V$. Future timestamps are used as
 1032 queries in the multi-head attention, and the number of variables corresponds to the output dimension
 1033 of the MLP. As for the hyperparameters, the hidden dimension size is set to 128, the number of
 1034 reference points is 32, and the number of scale levels used by ReIMTS is 2 on all five datasets. The
 1035 learning rate is 1×10^{-3} .

1036 **ReIMTS+GRU-D** uses GRU-D (Che et al., 2018) as backbones. GRU-D encodes input IMTS
 1037 into temporal representations for both lookback and future timestamps, as described in Eq.16 of
 1038 its paper. Therefore, it belongs to the case $\mathbf{E}^n = \mathbf{E}_{\text{time}}^n$ in Eq. 9 and learns multi-scale temporal
 1039 representations. For the decoder of GRU-D, it consists of an MLP maps temporal representations of
 1040 shape $(L_S + L_Q) \times D$ into time series $(L_S + L_Q) \times V$. Therefore, future timestamps are included
 1041 in the temporal representations, and the number of variables corresponds to the output dimension
 1042 of the linear layer. To handle irregularities, GRU-D replaces padding values with the last observed
 1043 values before processing through a GRU unit. After generating the predicted series, it uses a mask
 1044 to retain only the observed and predicted values. As for the hyperparameters, since the original
 1045 paper of GRU-D set the hidden dimension size to 100, we additionally include this setting during
 1046 hyperparameter searching. The hidden dimension size is set to 100, 64, 100, 64, and 32 on dataset
 1047 MIMIC-III, MIMIC-IV, PhysioNet’12, Human Activity, and USHCN, respectively. The number of
 1048 scale levels used by ReIMTS is set to 2 on all datasets except MIMIC-III, which adopts 3 levels
 1049 instead. The learning rate is 1×10^{-3} .

1050 **ReIMTS+Raindrop** uses Raindrop (Zhang et al., 2021) as backbones. Raindrop encodes input
 1051 IMTS into observation representations, as described in Eq.2 of its paper. Therefore, it belongs to the
 1052 case $\mathbf{E}^n = \mathbf{E}_{\text{obs}}^n$ in Eq. 10 during implementation and learns multi-scale observational representations.
 1053 Other modifications include reducing the number of propagation layers from two to one and removing
 1054 the final transformer encoder layer. For the decoder of Raindrop, it is a linear layer that maps then
 1055 rearranges variable representations of shape $V \times D$ into a time series with shape $L_Q \times V$. The
 1056 variable IDs are learned within these representations, and the forecast length is the output dimension
 1057 of the linear layer. To handle irregularities, it employs the mask on learned representations to retain
 1058 only the positions corresponding to actual input observations. As for the hyperparameters, the number
 1059 of layers used by Raindrop backbone is set to 2 on all five datasets. The hidden dimension size is
 1060 set to 64, 1, 16, 64, and 16 on dataset MIMIC-III, MIMIC-IV, PhysioNet’12, Human Activity, and
 1061 USHCN, respectively. The number of scale levels used by ReIMTS is set to 2 on all five datasets.
 1062 The learning rate is 1×10^{-3} .

1063 **ReIMTS+PrimeNet** uses PrimeNet (Chowdhury et al., 2023) as backbones. PrimeNet encodes
 1064 input IMTS into temporal representations for both lookback and future timestamps, as described
 1065 in Eq.2 in its paper. Therefore, it belongs to the case $\mathbf{E}^n = \mathbf{E}_{\text{time}}^n$ in Eq. 9 and learns multi-scale
 1066 temporal representations. We disable the patch splitting operation in the original PrimeNet. For the
 1067 decoder of PrimeNet, it is also an MLP maps temporal representations of shape $(L_S + L_Q) \times D$ into
 1068 time series $(L_S + L_Q) \times V$. Future timestamps are included in the temporal representations, and the
 1069 number of variables corresponds to the output dimension of the linear layer. To handle irregularities,
 1070 it retains only the observed and predicted values after obtaining output series by applying the mask.
 1071 As for the hyperparameters, the hidden dimension size is set to 256, 256, 256, 256, and 128 on dataset
 1072 MIMIC-III, MIMIC-IV, PhysioNet’12, Human Activity, and USHCN, respectively. The number of
 1073 scale levels used by ReIMTS is set to 2 on all five datasets. The learning rate is 1×10^{-4} .

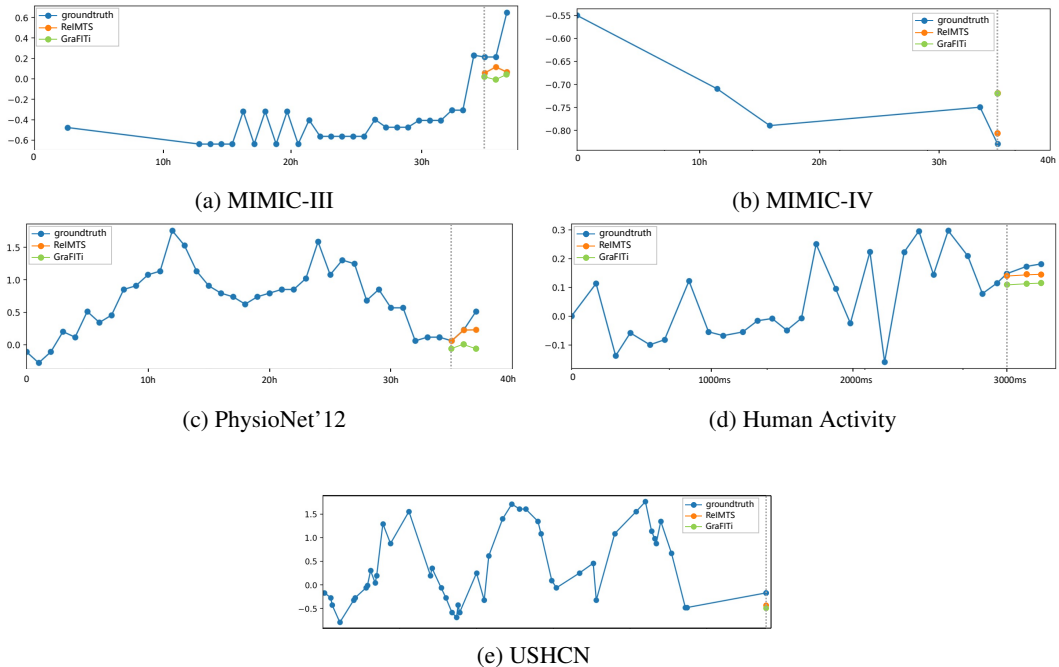
1074 **ReIMTS+TimeCHEAT** uses TimeCHEAT (Liu et al., 2025) as backbones. TimeCHEAT is based
 1075 on GraFITi (Yalavarthi et al., 2024) and simultaneously learns temporal, variable, and observation
 1076 representations, as described from Eq.3 to Eq.10 of its paper. We found that sharing variable
 1077 embeddings across different scale levels is sufficient during our experiments. Therefore, it belongs to
 1078 the case $\mathbf{E}^n = \mathbf{E}_{\text{var}}^n$ in Eq. 11 during implementation and learns multi-scale variable representations.
 1079 The patch splitting operation in orginal TimeCHEAT is disabled, and the final transformer encoding

1080 is discarded. Other settings remain the same. For the decoder of TimeCHEAT, it is a linear
 1081 layer that decodes and squeezes representations of shape $(L_S + L_Q) \times V \times (3D)$ into time series
 1082 $(L_S + L_Q) \times V$. These representations are obtained by concatenating temporal, variable, and
 1083 observational representations along the hidden dimension, each repeated and expanded to shape
 1084 $(L_S + L_Q) \times V \times D$. Therefore, future timestamps are included in the temporal representations,
 1085 while variable IDs are included in the variable ones. To handle irregularities, it uses a bipartite graph
 1086 approach like GraFITi, which removes all padding values and transform inputs into bipartite graphs.
 1087 As for the hyperparameters, the number of layers is set to 2, 2, 4, 2, and 4 on dataset MIMIC-III,
 1088 MIMIC-IV, PhysioNet'12, Human Activity, and USHCN, respectively. The hidden dimension size is
 1089 set to 128, 64, 32, 32, and 64 on dataset MIMIC-III, MIMIC-IV, PhysioNet'12, Human Activity, and
 1090 USHCN, respectively. The number of scale levels used by ReIMTS is set to 2 on all five datasets.
 1091 The learning rate is 1×10^{-3} .

1092 **ReIMTS+GraFITi** uses GraFITi (Yalavarthi et al., 2024) as backbones. GraFITi simultaneously
 1093 learns temporal, variable, and observation representations, as described from Eq.11 to Eq.13 of its
 1094 paper. During our implementation, we only transfer variable representations across different scale
 1095 levels. Therefore, it belongs to the case $E^n = E_{var}^n$ in Eq. 11 during implementation and learns
 1096 multi-scale variable representations. For the decoder of GraFITi, please refer to the descriptions
 1097 of TimeCHEAT's decoder above. To handle irregularities, it uses a bipartite graph approach that
 1098 removes all padding values and transform inputs into bipartite graphs. As for the hyperparameters,
 1099 the number of layers is set to 4, 1, 1, 4, and 1 on dataset MIMIC-III, MIMIC-IV, PhysioNet'12,
 1100 Human Activity, and USHCN, respectively. The hidden dimension size is set to 128, 64, 128, 128,
 1101 and 32 on dataset MIMIC-III, MIMIC-IV, PhysioNet'12, Human Activity, and USHCN, respectively.
 1102 The number of scale levels used by ReIMTS is set to 2 on all datasets except PhysioNet'12, which
 1103 adopts 3 levels instead. The learning rate is 1×10^{-3} .

D VISUALIZATION

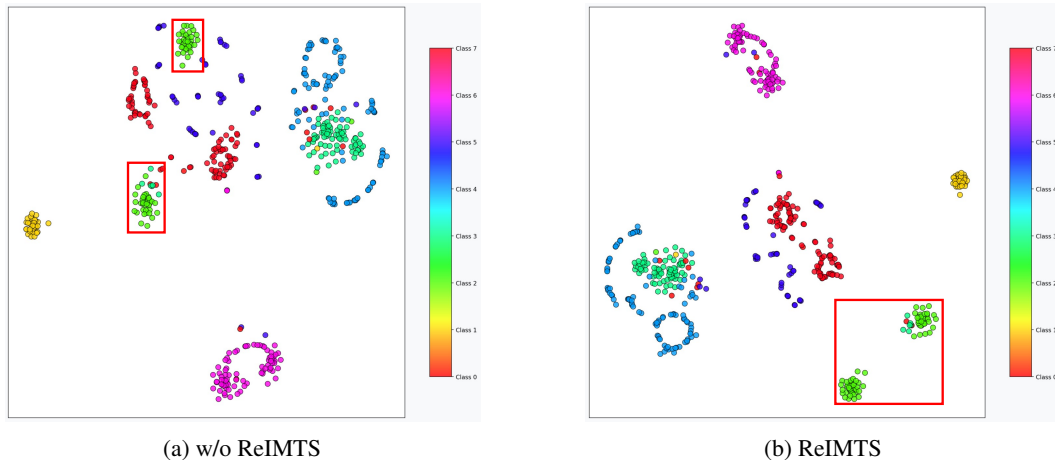
D.1 FORECASTING RESULTS



1132 Figure 7: Visualization of forecast results on all five datasets, under the same settings as in Table 2.
 1133 Compared to original backbone GraFITi (in green), ReIMTS (in orange) is closer to the ground truth
 (in blue).

1134 We visualize the forecasting results of our proposed ReIMTS when using GraFITi as its backbone,
 1135 and also ones from the original GraFITi model, as depicted in Figure 7. The forecast settings are
 1136 exactly the same as in Table 2, which means the lookback window length is set to 36 hours for
 1137 MIMIC-III, MIMIC-IV, and PhysioNet’12, 3000 milliseconds for Human Activity, and 3 years for
 1138 USHCN. The goal is to predict next 300ms for Human Activity, and 3 timestamps for other datasets.
 1139 As can be seen, ReIMTS is closer to the ground truth value. The detailed information for these
 1140 visualized time series is also provided below. For MIMIC-III, the time series is the 58th variable
 1141 from the 2029th sample of test set. For MIMIC-IV, the time series is the 6th variable from the 537th
 1142 sample of test set. For PhysioNet’12, the time series is the 6th variable from the 663rd sample of
 1143 test set. For Human Activity, the time series is the 1st variable from the 1st sample of test set. For
 1144 USHCN, the time series is the 4th variable from the 2nd sample of test set.

1145 D.2 MULTI-SCALE REPRESENTATIONS



1148
 1149 Figure 8: The t-SNE visualization of multi-scale representations in ReIMTS+GRU-D on classification
 1150 dataset PAM. Red boxes indicate the region of interest, which mainly contain samples from class 2. (a)
 1151 Without ReIMTS, samples from class 2 are very close to ones from class 5 and 7. (b) After applying
 1152 ReIMTS, samples from class 2 are more distant from others, leading to improved performance. It
 1153 should be noted that class 3 and class 2 have similar colors, where samples from class 3 are mostly
 1154 outside of the region of interest.

1155 Since it’s hard to visualize the relationships between learned representations and forecasting accuracy,
 1156 we train ReIMTS+GRU-D on classification task instead for visualization, as depicted in Figure 8
 1157 where colored points represent test set samples. GraFITi is not originally designed for classification
 1158 task, so we choose the classic and widely acknowledged GRU-D as backbones for ReIMTS. Widely
 1159 studied dataset PAM (Reiss & Stricker, 2012) is used, which contains 8 class labels. We follow the
 1160 preprocessing scripts of Raindrop (Zhang et al., 2021) and split the train/val/test sets adhere to ratio
 1161 8:1:1. Other training protocols are the same as forecasting training in Table 3. As can be seen in
 1162 Figure 8 (a), when learning without ReIMTS, samples from class 2 are very close to ones from class
 1163 5 and 7. The test set performance is 84.14% in precision, 78.04% in recall, and 75.03% in F1. After
 1164 applying ReIMTS in Figure 8 (b), samples from class 2 are more distant from others multi-scale
 1165 representations. The test set performance is improved to 86.74% in precision, 84.04% in recall, and
 1166 82.44% in F1.

1167 E BASELINE DETAILS

1168 We briefly introduce each baseline model along with their key hyperparameter settings here. The
 1169 search of hyperparameters aims to minimize the loss on validation sets. The number of layers is
 1170 searched within 1, 2, 3, and 4, the hidden dimension size is searched within 16, 32, 64, 128, 256,
 1171 and 512, and the patch length is searched in 3, 6, 10, 12, 24, 50, 90, 180, 300, 360, and 500. Unless
 1172 otherwise specified, we use a batch size of 16 for USHCN, and 32 for others. However, if the model

1188 cannot be trained using 24 GB of GPU memory, we recursively halve the batch size until training is
 1189 possible. Number of epochs, early stopping patience, random seeds, and learning rates have been
 1190 described in Section 5.1.3. We aim to use the same hyperparameters for learning rate and special loss
 1191 functions, as specified in their original papers and codes, whenever available. For all classification
 1192 models, we replace the final softmax layer with a linear layer to enable forecasting.
 1193

1194 **E.1 METHODS FOR MTS**
 1195

1196 **MOIRAI** (Woo et al., 2024) is a pretraining model for time series forecasting. We use the small
 1197 version of the provided pretrained configurations and weights, comprising 6 layers with hidden
 1198 dimension 384. We finetune the model on IMTS datasets with learning rate of 1×10^{-4} .
 1199

1200 **Ada-MSHyper** (Shang et al., 2024) uses hypergraphs for temporal multi-scale learning in MTS
 1201 forecasting. The window size for multiscale is 4. The learning rate is 1×10^{-3} . We also use its
 1202 node and hyperedge constrained loss function for training. The number of layers is set to 1, 1, 2, 1,
 1203 and 1 on dataset MIMIC-III, MIMIC-IV, PhysioNet’12, Human Activity, and USHCN, respectively.
 1204 The hidden dimension size is set to 32, 256, 256, 512, and 512 on dataset MIMIC-III, MIMIC-IV,
 1205 PhysioNet’12, Human Activity, and USHCN, respectively.
 1206

1207 **Autoformer** (Wu et al., 2021) is a transformer variant with auto-correlation decomposition for
 1208 MTS forecasting. The attention factor is 3. The learning rate is 1×10^{-3} . The number of layers is set
 1209 to 4, 2, 1, 1, and 1 on dataset MIMIC-III, MIMIC-IV, PhysioNet’12, Human Activity, and USHCN,
 1210 respectively. The hidden dimension size is set to 32, 32, 64, 512, and 512 on dataset MIMIC-III,
 1211 MIMIC-IV, PhysioNet’12, Human Activity, and USHCN, respectively.
 1212

1213 **Scaleformer** (Shabani et al., 2022) is a coarse-to-fine multi-scale framework for transformer
 1214 models in MTS forecasting. We adopt its best-performing backbone evaluated in original paper,
 1215 Autoformer, in our benchmark. The scale factor is 2. The attention factor is 3. The number of
 1216 encoder layers is 2. The number of decoder layers is 1. The number of total layers is set to 4, 1, 1, 1,
 1217 and 2 on dataset MIMIC-III, MIMIC-IV, PhysioNet’12, Human Activity, and USHCN, respectively.
 1218 The hidden dimension size is set to 128, 256, 64, 256, and 32 on dataset MIMIC-III, MIMIC-IV,
 1219 PhysioNet’12, Human Activity, and USHCN, respectively. The learning rate is 1×10^{-3} .
 1220

1221 **TimesNet** (Wu et al., 2022) uses 2-D variantant modeling for MTS analysis. The attention factor
 1222 is 3. The dimension for FCN is 32. The learning rate is 1×10^{-3} . The number of layers is set to
 1223 1, 4, 1, 1, and 1 on dataset MIMIC-III, MIMIC-IV, PhysioNet’12, Human Activity, and USHCN,
 1224 respectively. The hidden dimension size is set to 256, 128, 128, 32, and 32 on dataset MIMIC-III,
 1225 MIMIC-IV, PhysioNet’12, Human Activity, and USHCN, respectively.
 1226

1227 **NHITS** (Challu et al., 2023) is a multi-scale model with hierarchical interpolation technique
 1228 for MTS forecasting. The learning rate is 1×10^{-3} . The hidden dimension size is set to 64, 32,
 1229 32, 512, and 128 on dataset MIMIC-III, MIMIC-IV, PhysioNet’12, Human Activity, and USHCN,
 1230 respectively.
 1231

1232 **PatchTST** (Nie et al., 2022) leverages patching in transformer for MTS forecasting. The patch
 1233 lengths are 12, 90, 6, 300 and 10 for MIMIC-III, MIMIC-IV, PhysioNet’12, Human Activity, and
 1234 USHCN, respectively. The number of encoder layers is 3. The attention factor is 3. The number of
 1235 heads in attention is 16. The learning rate is 1×10^{-4} . The hidden dimension size is set to 128, 128,
 1236 256, 512, and 512 on dataset MIMIC-III, MIMIC-IV, PhysioNet’12, Human Activity, and USHCN,
 1237 respectively.
 1238

1239 **Leddam** (Yu et al., 2024) uses learnable seasonal-trend decomposition for MTS forecasting. The
 1240 learning rate is 1×10^{-3} . The number of layers is set to 2, 4, 2, 1, and 1 on dataset MIMIC-III,
 1241 MIMIC-IV, PhysioNet’12, Human Activity, and USHCN, respectively. The hidden dimension size is
 1242 set to 32, 32, 128, 512, and 512 on dataset MIMIC-III, MIMIC-IV, PhysioNet’12, Human Activity,
 1243 and USHCN, respectively.
 1244

1242 **Pathformer** (Chen et al., 2023) is a multi-scale transformer with multi patch size aggregation.
 1243 Since Pathformer does not support splitting irregular time series into patches of different lengths,
 1244 the number of layers is fixed as 1. The hidden dimension size is set to 32, 16, 32, 16, and 16 on
 1245 dataset MIMIC-III, MIMIC-IV, PhysioNet’12, Human Activity, and USHCN, respectively. The patch
 1246 lengths are 12, 360, 6, 300, and 10 for MIMIC-III, MIMIC-IV, PhysioNet’12, Human Activity, and
 1247 USHCN, respectively. The learning rate is 1×10^{-3} .

1248 **Crossformer** (Zhang & Yan, 2022) learns cross-dimensional dependencies for MTS forecasting.
 1249 The segment lengths are 12, 360, 6, 300, and 3 for MIMIC-III, MIMIC-IV, PhysioNet’12, Human
 1250 Activity, and USHCN respectively. The learning rate is 1×10^{-3} . The number of encoder layers
 1251 is set to 2. The hidden dimension size is set to 32, 32, 128, 512, and 512 on dataset MIMIC-III,
 1252 MIMIC-IV, PhysioNet’12, Human Activity, and USHCN, respectively.

1253 **TimeMixer** (Wang et al., 2023) uses seasonal-trend decomposition at each sampling scale level.
 1254 The down sampling windows are 12, 360, 6, 300, and 10 for MIMIC-III, MIMIC-IV, PhysioNet’12,
 1255 Human Activity, and USHCN, respectively. The number of encoder layer is 3. The dimension
 1256 for feed-forward layer is 32. The learning rate is 1×10^{-2} . The number of total layers is set to
 1257 4, 2, 1, 1, and 1 on dataset MIMIC-III, MIMIC-IV, PhysioNet’12, Human Activity, and USHCN,
 1258 respectively. The hidden dimension size is set to 32, 32, 64, 16, and 16 on dataset MIMIC-III,
 1259 MIMIC-IV, PhysioNet’12, Human Activity, and USHCN, respectively.

1261 E.2 METHODS FOR IMTS

1262 **PrimeNet** (Chowdhury et al., 2023) is an IMTS pretraining model. Since the provided weights
 1263 are specific to datasets with 41 variables, we retrain the model on all datasets. The patch lengths are
 1264 12, 180, 6, 300, and 10 for MIMIC-III, MIMIC-IV, PhysioNet’12, Human Activity, and USHCN
 1265 respectively. The number of heads in attention is 1. The learning rate is 1×10^{-4} . The hidden
 1266 dimension size is set to 32, 32, 128, 128, and 256 on dataset MIMIC-III, MIMIC-IV, PhysioNet’12,
 1267 Human Activity, and USHCN, respectively.

1268 **SeFT** (Horn et al., 2020) is a set-based method for IMTS classification. The dropout rate is 0.1.
 1269 The learning rate is 1×10^{-3} . The number of layers is set to 2, 2, 4, 4, and 4 on dataset MIMIC-III,
 1270 MIMIC-IV, PhysioNet’12, Human Activity, and USHCN, respectively. The hidden dimension size is
 1271 set to 256, 64, 32, 128, and 256 on dataset MIMIC-III, MIMIC-IV, PhysioNet’12, Human Activity,
 1272 and USHCN, respectively.

1273 **mTAN** (Shukla & Marlin, 2020) converts IMTS to reference points for IMTS classification. The
 1274 number of reference points is 32 on MIMIC-III and 8 on the rest datasets. The hidden dimension size
 1275 is set to 32, 64, 64, 64, and 128 on dataset MIMIC-III, MIMIC-IV, PhysioNet’12, Human Activity,
 1276 and USHCN, respectively. The learning rate is 1×10^{-3} .

1277 **NeuralFlows** (Biloš et al., 2021) is an efficient alternative to Neural ODE in IMTS analysis. The
 1278 number of flow layers is 2. The latent dimension is 20. The hidden dimension for time is 8. The
 1279 number of hidden layers is 3. The learning rate is 1×10^{-3} .

1280 **CRU** (Schirmer et al., 2022) uses continuous recurrent units for IMTS analysis. The hidden
 1281 dimension is 20. The learning rate is 1×10^{-3} .

1282 **TimeCHEAT** (Liu et al., 2025) uses channel-dependent within patches and channel-independent
 1283 among patches. The patch lengths are 12, 180, 6, 300, and 10 for MIMIC-III, MIMIC-IV, Phy-
 1284 sioNet’12, Human Activity, and USHCN respectively. The number of attention heads is 4. The
 1285 learning rate is 1×10^{-3} . The number of layers is set to 1, 1, 1, 2, and 1 on dataset MIMIC-III,
 1286 MIMIC-IV, PhysioNet’12, Human Activity, and USHCN, respectively. The hidden dimension size is
 1287 set to 32, 32, 32, 64, and 32 on dataset MIMIC-III, MIMIC-IV, PhysioNet’12, Human Activity, and
 1288 USHCN, respectively.

1289 **GNeuralFlow** (Mercatali et al., 2024) enhances NeuralFlows with graph neural networks for IMTS
 1290 analysis. The flow model uses ResNet. The number of flow layers is 2. The latent dimension for

1296 input is 20. The latent dimension for time is 8. The number of hidden layers is 3. The learning rate is
 1297 1×10^{-3} .
 1298

1299 **GRU-D** (Che et al., 2018) adapts GRUs for IMTS classification. The learning rate is 1×10^{-3} .
 1300 Since the original paper of GRU-D set the hidden dimension size to 100, we additionally include this
 1301 setting during hyperparameter searching. The hidden dimension size is set to 100, 32, 100, 100, and
 1302 256 on dataset MIMIC-III, MIMIC-IV, PhysioNet’12, Human Activity, and USHCN, respectively.
 1303

1304 **Raindrop** (Zhang et al., 2021) models time-varying variable dependencies for IMTS classification.
 1305 The learning rate is 1×10^{-4} . The number of layers is set to 1, 2, 1, 1, and 2 on dataset MIMIC-III,
 1306 MIMIC-IV, PhysioNet’12, Human Activity, and USHCN, respectively. The hidden dimension size is
 1307 set to 32, 32, 32, 32, and 32 on dataset MIMIC-III, MIMIC-IV, PhysioNet’12, Human Activity, and
 1308 USHCN, respectively.

1309 **tPatchGNN** (Zhang et al., 2024) processes IMTS into patches and use graph neural networks
 1310 for IMTS forecasting. The patch lengths are 12, 360, 6, 300, and 10 for MIMIC-III, MIMIC-IV,
 1311 PhysioNet’12, Human Activity, and USHCN, respectively. The number of heads in attention is 1.
 1312 The learning rate is 1×10^{-3} . The number of layers is set to 4, 2, 4, 4, and 1 on dataset MIMIC-III,
 1313 MIMIC-IV, PhysioNet’12, Human Activity, and USHCN, respectively. The hidden dimension size is
 1314 set to 64, 32, 64, 64, and 256 on dataset MIMIC-III, MIMIC-IV, PhysioNet’12, Human Activity, and
 1315 USHCN, respectively.
 1316

1317 **Hi-Patch** (Luo et al., 2025) implements hierarchical graph fusion inside backbone. The patch
 1318 lengths are 12, 360, 6, 300, and 10 for MIMIC-III, MIMIC-IV, PhysioNet’12, Human Activity, and
 1319 USHCN, respectively. The number of attention heads is 1. The learning rate is 1×10^{-3} . The number
 1320 of layers is set to 4, 1, 4, 4, and 2 on dataset MIMIC-III, MIMIC-IV, PhysioNet’12, Human Activity,
 1321 and USHCN, respectively. The hidden dimension size is set to 32, 64, 32, 128, and 256 on dataset
 1322 MIMIC-III, MIMIC-IV, PhysioNet’12, Human Activity, and USHCN, respectively.
 1323

1324 **Warpformer** (Zhang et al., 2023a) uses warping for multiscale modeling in IMTS classification.
 1325 The number of heads is 1. The dropout rate is 0. The learning rate is 1×10^{-3} . The number of
 1326 layers is set to 4, 1, 1, 3, and 1 on dataset MIMIC-III, MIMIC-IV, PhysioNet’12, Human Activity,
 1327 and USHCN, respectively. The hidden dimension size is set to 64, 64, 64, 64, and 128 on dataset
 1328 MIMIC-III, MIMIC-IV, PhysioNet’12, Human Activity, and USHCN, respectively.
 1329

1330 **HD-TTS** (Marisca et al., 2024) implements both variable and temporal multi-scale inside backbone.
 1331 The number of rnn layers is 4. The number of pooling layers is 1. The learning rate is 1×10^{-3} .
 1332 The hidden dimension size is set to 64, 64, 256, 128, and 64 on dataset MIMIC-III, MIMIC-IV,
 1333 PhysioNet’12, Human Activity, and USHCN, respectively.
 1334

1335 **GraFITi** (Yalavarthi et al., 2024) uses bipartite graphs for IMTS forecasting. The number of
 1336 heads in attention is 4. The learning rate is 1×10^{-3} . The number of layers is set to 4, 1, 2, 4,
 1337 and 1 on dataset MIMIC-III, MIMIC-IV, PhysioNet’12, Human Activity, and USHCN, respectively.
 1338 The hidden dimension size is set to 128, 32, 32, 32, and 128 on dataset MIMIC-III, MIMIC-IV,
 1339 PhysioNet’12, Human Activity, and USHCN, respectively.
 1340

F THE USE OF LARGE LANGUAGE MODELS

1341 We use Large Language Models (LLMs) to polish writing only. Specifically, we write all contents
 1342 ourselves, then use LLMs to check for any possible grammar mistakes or incorrect usage of words.
 1343 We have not used LLMs for any other purpose.
 1344

1345
 1346
 1347
 1348
 1349